

THE ${}^3\text{He}(\alpha, \gamma){}^7\text{Be}$ REACTION
AT LOW ENERGIES

thesis by
John Lawrence Osborne

In Partial Fulfillment of the Requirements
For the Degree of
Doctor of Philosophy

California Institute of Technology
Pasadena, California
1983

(Submitted June 24, 1982)

ACKNOWLEDGEMENTS

It is difficult to find the words to express my sincere appreciation to the staff, students and faculty of the Kellogg Radiation Laboratory for providing a stimulating and encouraging atmosphere in which to work, to study and to play. In particular I wish to thank Professor C. A. Barnes for his patient instruction and guidance, Professor W. A. Fowler for his continuing interest in these experiments and Professor R. W. Kavanagh for his remarkable ability to draw unexpected amounts of beam from accelerators and knowledge from students. Special thanks go to Professor P. D. Parker of Yale University for the conception and design of the activity experiment and to Professor A. J. Howard of Trinity College, Dr. G. J. Mathews, Dr. J. L. Zyskind and R. M. Kremer for their invaluable assistance in the design, maintenance and operation of the experiments during the interminable hours of data collection. This work has greatly benefitted from many informative discussions with Professor S. E. Koonin, Professor T. A. Tombrello, Dr. H. S. Wilson, R. D. Williams and Dr. H. Friederich.

Finally, I want to extend my sincere thanks to Dr. Martin Weiss of USC Medical School for his innovative skill which made the completion of this work possible. This research was supported in part by the National Science Foundation under Grant No. PHY79-23638.

ABSTRACT

Cross sections for the ${}^3\text{He}(\alpha,\gamma){}^7\text{Be}$ reaction have been measured at several energies from $E_{cm}=165$ to 1200 keV by counting prompt γ rays from a windowless, differentially pumped, recirculating, ${}^3\text{He}$ gas target. The cross-section factor $S_{34}(E_{cm})$ and branching ratio γ_1/γ_0 were determined at each energy. Absolute cross sections were measured at $E_{cm}=947$ and 1255 keV by counting the γ rays from the ${}^7\text{Be}$ produced in a ${}^3\text{He}$ gas cell with a Ni entrance foil. The inferred zero-energy intercept of the cross-section factor is $S_{34}(0)=0.52\pm 0.03$ keV-barn. This value is in good agreement with the previous measurements of Parker and Kavanagh and Nagatani *et al.*, but disagrees substantially with the recently published measurement of Kräwinkel *et al.* from Münster. The relationship between the present measurements and several theoretical calculations, and the effect of the extrapolated cross section on the solar neutrino problem are discussed.

TABLE OF CONTENTS

	page
ACKNOWLEDGEMENTS	ii
ABSTRACT	iii
I. INTRODUCTION	
A. Solar Models	1
B. Solar Neutrino Problem	2
C. The ${}^3\text{He}(\alpha, \gamma){}^7\text{Be}$ Reaction	3
II. EXPERIMENTAL APPARATUS AND PROCEDURE	
A. Windowless Gas Target System	11
1. Target	11
2. Detection	12
3. Procedure	13
B. Gas-cell Activity Measurement	15
1. Target	15
2. Detection	15
3. Procedure	16
III. DATA ANALYSIS	19
A. Windowless Gas Target System	19
1. γ -ray Yield	22
2. Angular Distribution Function	22
3. Number of Beam Particles	23
4. Target Density	24
5. Detector Efficiency	25
6. Calculation of errors	26

TABLE OF CONTENTS (cont.)

B. Gas-cell Activity Measurement	28
1. γ -ray yield	30
2. Beam Energy	30
3. Current Integration	31
4. Target Density	31
5. Detector Efficiency	32
6. Calculation of errors	33
IV. RESULTS AND CONCLUSIONS	35
A. Experimental Results	35
B. Relation to theory	37
C. Astrophysical Implications	38
Appendix A: Calorimeter	40
Appendix B: Integration of γ-ray Yields	43
REFERENCES	45
TABLES	48
1. WINDOWLESS TARGET RUN PARAMETERS	48
2. EMPIRICAL EFFICIENCY FUNCTION	51
3. SYSTEMATIC ERRORS	52
4. ACTIVITY MEASUREMENT RUN PARAMETERS	54
5. RESULTS	56
6. THEORETICAL FITS	59
7. CALORIMETER CALIBRATION	61

TABLE OF CONTENTS (cont.)

FIGURES	63
1. ENERGY LEVEL DIAGRAM	63
2. RESULTS OF PREVIOUS EXPERIMENTS	65
3. THEORETICAL CALCULATIONS	67
4. WINDOWLESS GAS-TARGET SYSTEM	69
5. WINDOWLESS TARGET	71
6. PARTICLE SPECTRA	73
7. DETECTOR ELECTRONICS	75
8. WINDOWLESS TARGET BEAMLINE	77
9. GAS CELL	79
10. TARGET CELL GAS MANIFOLD	81
11. $^{24}\text{Mg}(\alpha,\gamma)^{28}\text{Si}$ FOIL THICKNESS MEASUREMENT	83
12. $^{14}\text{N}(\alpha,\gamma)^{18}\text{F}$ FOIL THICKNESS MEASUREMENT	85
13. DIRECT-CAPTURE γ -RAY SPECTRA	87
14. γ -RAY DETECTION EFFICIENCIES	89
15. TOTAL DETECTION EFFICIENCY	91
16. CATCHER FOIL SPECTRUM	93
17. PROMPT γ -RAY SPECTRUM	95
18. RESULTS	97
19. CALORIMETER	99
20. CALORIMETER CONTROLLER CIRCUIT	101
21. CALORIMETER CURRENT DECAY	103

I. INTRODUCTION

A. Solar Models

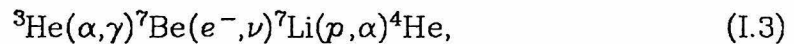
Nuclear Astrophysics was born in 1939 with the pioneering work of Hans Bethe (Be39) in which he showed that the production of energy in our sun could come from the fusion of four protons into ${}^4\text{He}$ using ${}^{12}\text{C}$ as a catalyst in what has become known as the CNO cycle. The 1951 discovery of the reaction



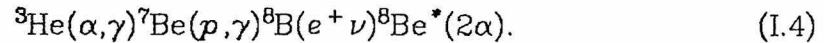
by Fowler and Lauritsen (Fo51), provided the endpoint for the direct combination of protons into ${}^4\text{He}$ at a temperature below that required for the CNO cycle. In 1958 Holmgren and Johnston (Ho59) found the cross section for



to be ~ 100 times larger than the value being used in the solar model calculations of Salpeter (Sa52) and Burbidge, Burbidge, Fowler and Hoyle (Bu57). Fowler (Fo58) and Cameron (Ca58) independently calculated that, at solar temperatures, reaction (I.2) would compete with reaction (I.1) to complete the Proton-Proton Chain through either



or



Both Cameron and Fowler recognized that the energetic neutrinos from the decay of ${}^8\text{B}$ in reaction chain (I.4) could provide an experimental test of solar models, if this branch were strong enough. Although the mean free path for particles and γ rays is far too short for information about the reaction processes in the interior of the sun to propagate to the outside, neutrinos, with their small interaction cross sections, will escape. Davis (Da55) had developed a sensitive neutrino detector based on the endoergic neutrino-capture reaction,



which has an interaction cross section proportional to the square of the neutrino energy minus the threshold energy, 0.81 MeV. For neutrinos with energy above 5.8 MeV, the superallowed transition to the isobaric analog state in ${}^{37}\text{Ar}$ is possible, further enhancing the yield from ${}^8\text{B}$ neutrinos.

B. Solar Neutrino Problem

Using the neutrino-flux calculations from the 1963 solar model of Bahcall, Fowler, Iben and Sears (Ba63), Bahcall and Davis (Ba64 and Da64) demonstrated the theoretical and experimental feasibility of an experiment to measure the solar-neutrino flux. By 1968, the Brookhaven solar neutrino experiment, a 100,000 gallon tank of perchlorethylene, began collecting data in the Homestake mine at Lead, South Dakota, 4800 feet below the surface to reduce the background induced by cosmic rays. With improved measurements of the important cross sections for ${}^3\text{He}(\alpha, \gamma){}^7\text{Be}$ (Pa63 and Na69), ${}^7\text{Be}(p, \gamma){}^8\text{B}$ (Pa66) and ${}^3\text{He}({}^3\text{He}, 2p){}^4\text{He}$ (Ba67) and

improved solar model programs, a theoretical neutrino-capture rate of 7.5 ± 3.0 SNU (Solar Neutrino Unit, 1 SNU = 10^{-36} captures per ^{37}Cl atom per second) was calculated by Bahcall *et al.* (Ba68). The discrepancy between this theoretical value and the <3 SNU that was reported by Davis, Harmer and Hoffman (Da68) has become known as the solar neutrino problem. Refinements in solar models and in the experimental technique have had little effect on the magnitude of this problem; the most recent theoretical and experimental capture rates are 7.6 ± 3.3 ($3\text{-}\sigma$ error) (Ba82) and 2.2 ± 0.3 SNU (Cl80). Most of the explanations that have been offered to resolve the problem fit into three categories; those which require modifications to the structure or evolution of solar models, such as Fowler's suggestion that the central temperature of the sun may oscillate, and that at the present time the temperature is at a minimum (Fo72); changes in the underlying particle physics, as in the quark catalysis of Libbey and Thomas (Li69) or neutrino oscillations, suggested by Gribov and Pontecorvo (Gr69), and errors in the measured nuclear reaction rates, as suggested by Fowler (Fo72) and others.

C. The $^3\text{He}(\alpha, \gamma)^7\text{Be}$ Reaction

The energy level diagram for the $^3\text{He}+^4\text{He}$ system is shown in figure 1. The entrance channel has a Q-value of 1586.4 keV relative to the ground state of ^7Be . Since ^7Be has no energy levels between the first excited state at 429 keV and the $\frac{7}{2}^-$ state at 4.57 MeV, the capture reaction at energies below $E_{cm} = 2500$ keV will proceed directly with the emission of a γ ray (γ_0 or γ_1) to either the ground or first excited state.

Because of the coulomb barrier, the cross section for $^3\text{He}(\alpha, \gamma)^7\text{Be}$

decreases rapidly with energy below $E_{cm}=1000$ keV. At solar energies, the capture cross section is too low to be measured: approximately 1000 particle coulombs of beam would be required to produce a single capture at $E_{\alpha}=40$ keV. Measurements of the cross section must be made at higher energies and extrapolated theoretically to the region of interest. For these extrapolations, it is convenient to use an expression in which the coulomb effect has been factored out, such as the cross-section factor,

$$S(E_{cm})=\sigma(E_{cm})E_{cm}e^{2\pi\eta}, \quad (I.6)$$

where η is the Sommerfeld parameter,

$$\eta=\frac{Z_1Z_2e^2}{h\nu}, \quad (I.7)$$

Z_1 and Z_2 are the projectile and target charges and ν is their relative velocity. For the ${}^3\text{He}(\alpha,\gamma){}^7\text{Be}$ reaction at low energies, the cross-section factor reduces to

$$S_{34}(E_{cm})=\sigma(E_{cm})E_{cm}\exp\left[\frac{164.125}{\sqrt{E_{cm}}}\right], \quad (I.8)$$

with E_{cm} in keV.

The first experimental measurement of the cross section for ${}^3\text{He}(\alpha,\gamma){}^7\text{Be}$ was made by Holmgren and Johnston (Ho59). Their apparatus consisted of a gas cell filled with ${}^3\text{He}$ which an α beam from an electrostatic accelerator entered through a thin nickel foil. The cross section and S-factor were calculated from direct capture gamma rays which were collected using a 3x5-in. well-type NaI(Tl) detector, and no attempt was made to distinguish between the ground state and first excited state

transitions. Background was subtracted by performing the same experiment on the target filled with ^4He . The experimental uncertainty in this measurement was quite high, particularly at low energies, due to the large beam-energy spread (120 keV) caused by energy-loss straggling in the entrance foil and energy loss in the target itself. Using a linear extrapolation from the cross-section factors measured at $E_{cm}=200, 300$ and 400 keV, they determined a zero-energy intercept of $S(0)=1.2$ keV-b.

Christy and Duck (Ch61) and Tombrello and Phillips (To61) independently developed the theoretical model for the calculation of non-resonant, direct, radiative capture reactions. Their calculations were based on the assumption that the process involves a direct electromagnetic transition from the initial state to a final bound state. The cross section for this type of reaction is then found by calculating the matrix element, between the initial and final state wavefunctions, of the electromagnetic interaction Hamiltonian,

$$H_{int} = -\frac{1}{c}(\mathbf{j}\cdot\mathbf{A}), \quad (I.9)$$

where \mathbf{j} is the nuclear current density and \mathbf{A} is the vector potential of the photon field. Both calculations were simplified by considering only the electric-dipole component of the Hamiltonian; assuming that the capture would be dominated by a transition from an initial s-state to a final p-state. The initial-state was expressed in terms of coulomb wavefunctions for a hard-sphere potential with the nuclear radius adjusted to reproduce the experimentally observed elastic scattering phase shifts. Whittaker functions, adjusted to give the proper separation energies, were used for the final bound states. In both cases only the contributions to the

integrals from outside the nuclear volume were used. These calculations made no estimate of the absolute cross section for the reaction, since no estimate is made of the reduced width of the ${}^3\text{He}+{}^4\text{He}$ cluster component of the ${}^7\text{Be}$ wavefunction. These reduced widths, which are independent of initial state energy, are left as fitting parameters to normalize the calculation to experimental data. Experimental data for total cross section and branching ratio are thus sufficient to define both partial widths and to establish a unique extrapolation to zero energy. The results of both of these investigations were consistent with the data of Holmgren and Johnston, indicating a negative slope in the cross-section factor at low energies.

In 1963, Parker and Kavanagh (Pa63) reported a remeasurement of this cross section using detectors and apparatus similar to those used by Holmgren and Johnston. The accuracy of the experiment was improved by using thinner entrance foils and a shorter target cell. Using lineshape fits to the NaI(Tl) γ -ray spectra, the branching ratio was also calculated in this experiment. At this same time, Tombrello and Parker (To63) performed a more complete theoretical calculation. Using similar approximations for the initial- and final-state wavefunctions, they calculated not only the electric dipole part of the interaction Hamiltonian, but also the magnetic dipole and electric quadrupole components, fitting the initial-state wavefunction to the s-, p-, d- and f-wave phase shifts calculated from elastic scattering data. Again, the integrals were evaluated only in the extranuclear region. As shown in figure 2, the experimental data were in good agreement with this theoretical calculation, yielding a zero-energy intercept for the cross-section factor $S_{34}(0)=0.47\pm 0.05$ keV-b. As in the Holmgren experiment, there was still considerable uncertainty in

the low-energy measurements due to straggling and low count rate.

An experiment performed by Nagatani, Dwarakanath and Ashery (Na69) was the first to use a "windowless" target, in which the beam enters the gas target through a narrow tube, thereby eliminating the problem of energy loss and straggling in an entrance foil. Since beam current could not be integrated directly due to ionization and charge exchange in the relatively poor vacuum upstream of the target, a two-cup calorimeter was used, which provided 6% accuracy with a maximum current of $4\mu\text{A}$. The measurements from this experiment, shown in figure 2, were combined with those from the Parker and Kavanagh work to give an intercept of $S_{34}(0)=0.61\pm 0.07$ keV-b using a polynomial fit.

The continuing solar neutrino problem has prompted an experimental group in Münster (Kr79) to undertake a remeasurement of the low-energy ${}^3\text{He}(\alpha,\gamma){}^7\text{Be}$ cross section. Although their windowless target system is similar to that used by Nagatani *et al.*, the use of high-resolution, lithium-drifted germanium γ -ray detectors can improve the accuracy of the measurement by allowing an independent measurement of beam energy, by resolving the three γ rays of interest and by separating these γ rays from beam-related background. Some measurements have also been made by this group using a high-pressure, supersonic-jet, gas target, providing a direct determination of γ -ray angular distributions. Early reports from this group (Ro80) indicated either an energy dependent branching ratio or an energy independent cross-section factor, in direct disagreement with both the early experimental results and the theoretical calculations. These reports motivated the present investigation of the cross section and branching ratio for this reaction and spawned a renewed interest in the theoretical calculation of direct-capture cross

sections.

Kim, Izumoto and Nagatani (Ki81) employed three different techniques for their calculation of the ${}^3\text{He}(\alpha,\gamma){}^7\text{Be}$ cross section. The first method, involving a hard-core potential, was essentially the same as the previous calculation of Tombrello and Parker. For the partial widths, they used the same values obtained by Tombrello and Parker to fit the Parker and Kavanagh data. In the second calculation, the hard core potential was abandoned in favor of a more realistic, phenomenological Woods-Saxon potential, with the parameters adjusted to reproduce binding energies, elastic scattering data and the position and width of the $\frac{7}{2}^-$ state in ${}^7\text{Be}$. In the third approach, the orthogonality condition model (Sa68) was used to construct properly antisymmetrized ${}^3\text{He}+{}^4\text{He}$ cluster wavefunctions in a local gaussian potential including a spin orbit term to split the $\frac{3}{2}^-$ ground state and the $\frac{1}{2}^-$ first excited states of ${}^7\text{Be}$. The results of these three calculations are shown in figure 3. It can easily be seen that, despite the different methods of calculation, these curves qualitatively agree with each other and with the earlier calculation of Tombrello and Parker.

In a still more rigorous treatment, Liu, Kanada and Tang (Li81) have analyzed this reaction using a single channel (${}^3\text{He}+{}^4\text{He}$) resonating group calculation to obtain a correctly antisymmetrized seven-nucleon wavefunction in a non-local potential. In this calculation, only the electric-dipole component of the interaction was considered. The results of this calculation are shown in figure 3. Although there are no adjustable parameters in the calculation, this curve should provide a reasonable upper limit on the cross section, since only the single cluster channel was

considered.

Williams and Koonin (Wi81) found that the integrals for the matrix element, using the extranuclear approximation, could be evaluated analytically for the logarithmic derivative $\left[\frac{1}{S} \frac{dS}{dE} \right]$ of the cross-section factor at zero energy. Their calculated value of -0.575 MeV^{-1} , shown in figure 3 is also in good agreement with the previous theoretical calculations.

Kräwinkel *et al.* (Kr82) have now published the results of their windowless- and jet-target measurements which now agree with the previous experimental results for the energy dependence of branching ratio and cross-section factor. The normalization of their absolute measurements, however, gives a zero-energy intercept of $S_{34}(0)=0.30\pm 0.03 \text{ keV-b}$, 30-50% lower than the values presently adopted for solar-neutrino flux calculations.

The objectives of the present experiment were to determine the absolute cross section for the ${}^3\text{He}(\alpha,\gamma){}^7\text{Be}$ reaction at as low an energy as practical, and to make enough further measurements at higher energies to validate the theoretical extrapolation to solar temperatures. Because the entrance channel involves two isotopes of helium, it is necessary to use a gas target. Two independent measurements of the absolute cross section have been made. At low energies, the reaction cross section varies rapidly with energy (3.2% per keV at $E_{cm}=165 \text{ keV}$). For accurate measurements, a windowless target was used to avoid beam energy spread from energy-loss straggling in an entrance foil. The windowless target also allows higher beam currents and decreases beam-dependent background by eliminating the production of neutrons from the reaction

$^{13}\text{C}(\alpha, n)$ on carbon deposits on the entrance foil. At higher energies ($E_{cm} > 900$ keV) a gas cell target was employed. The problem of beam-dependent background was eliminated by counting the residual ^7Be activity instead of the prompt capture γ rays to measure the production. This method allows a direct measurement of the angle-integrated total cross section. On the other hand, the branching ratio (σ_1/σ_0), needed for the theoretical fit, cannot be measured with this technique, and accurate measurements at lower energies are not possible because of the low counting efficiency due to the 55-day half life and the 10% γ -ray branch of the decay of ^7Be .

II. EXPERIMENTAL APPARATUS AND PROCEDURE

A. Windowless Gas Target

1. Target

The windowless, differentially pumped, recirculating gas-target system is shown schematically in figure 4 and has been described previously by Dwarakanath and Winkler (Dw71). Although much of the apparatus is the same as that used in the measurement of Nagatani, Dwarakanath and Ashery (Na69), the use of a high-resolution γ -ray detector, low target pressure and a high current calorimeter significantly improves the experimental accuracy in the present measurement.

The target system consists of three chambers separated from each other and from the beam-line by a series of canals. The first chamber (A) is connected to a 6-inch oil diffusion pump. This chamber is separated from the beam-line by a 9.7-mm diameter water-cooled canal. Chambers A and B are connected by a 10-cm long stainless-steel canal 5.4 mm in diameter. On the upstream side of the canal is an electrically isolated 3.2-mm diameter tantalum aperture, and the first 5 cm of the canal contains a tantalum sleeve with an inside diameter of 4.7 mm. The foreline of the diffusion pump is connected to the second chamber (B) which is pumped by a Heraeus model 1600 Roots pump. The output of this pump is compressed by a Heraeus model 152 two-stage Roots pump and fed

through a heat exchanger and a liquid nitrogen cooled zeolite trap for gas purification. The gas is then fed into the third chamber (C), which is the gas target. Gas pressure in the target cell is monitored with a Model FA-160 Wallace and Tiernan pressure gauge, which reads 20 torr full scale. This gauge was calibrated against a mercury compound manometer. The target chamber (Figure 5) is 29-cm long from the upstream end of the entrance canal to the face of the calorimeter beamstop. The entrance canal to the gas target is a 3.2-cm long tantalum tube. The first 6 mm has a diameter of 4.3 mm, the remaining 2.6 mm has a diameter of 4.6 mm.

2. Detection

The γ -ray detector, a 100-cm³ lithium-drifted germanium crystal (Ge(Li)), Princeton Gamma-Tech serial number 1281, is located 13.3 cm from the center of the entrance canal. The front face of this Ge(Li) detector is 25 mm from the beam axis at an angle of 90° to the beam. The detector and the target chamber are surrounded by 10 cm of lead shielding to reduce γ -ray background. Between the detector and the target chamber is a 12-mm thick, 25-mm diameter lead aperture to limit the acceptance angle of the detector. The use of a high resolution γ -ray detector provides an accurate determination of beam energy since the capture γ -ray energy is dependent on the center of mass energy of the entrance channel. To obtain a homogeneous target and to isolate the detector from the entrance canal and beamstop requires an extended target and some of the advantage in using high-resolution γ -ray detectors is lost, since the γ -ray lines are broadened by a combination of beam-energy loss and doppler shift.

A 50-mm³, ruggedized, silicon surface-barrier detector, Ortec serial no. 19-452D, is located 13.6 cm from the beam at an angle of 45°. The acceptance angle of this detector is defined by two 0.127-mm thick tantalum apertures, a 1.0-mm vertical slit at 4.7 cm and a 0.62-mm circular hole at 12.7 cm from the center of the beam path. The particle detector was used to monitor gas contamination and to check beam current and target pressure. Typical particle spectra are shown in figure 6. A block diagram of the detector electronics is shown in figure 7.

3. Experimental Procedure

At low energies ($E_\alpha = 401$ to 1200 keV), 20 to 60 μA $^4\text{He}^+$ ion beams from the ONR-CIT JN Electrostatic Accelerator were used. The beams were energy analyzed with a 30° bending magnet. The layout of the beam line used in these measurements is shown in figure 8. The magnetic field strength of this magnet was monitored with a temperature stabilized Hall-effect probe. The energy resolution with this system was $\pm 0.3\%$. Two additional measurements were made at $E_\alpha = 1200$ and 2740 keV, using a 90° double-focusing analyzing magnet, giving energy resolution within 0.1%. At 2740 keV, the 1- μA $^4\text{He}^+$ beam was prepared with the ONR-CIT EN tandem accelerator. Beam energies were chosen at minima in the $^{13}\text{C}(\alpha, n)$ yield function to reduce neutron-induced background and to protect the Ge(Li) detector. Conventional current integration is not possible in windowless targets because of ionization of the low pressure gas in the target and upstream of the entrance canal. Beam current was integrated using the calorimeter described in detail in appendix A. This calorimeter allowed higher beam currents than were used in the Nagatani experiment. As a result, gas-target pressure could be reduced, thereby

decreasing beam energy loss and straggling in the target.

The low-energy measurements were made in groups of 2 to 4 different energies. During each group of measurements, the detector positions, bias voltages and the calorimeter base temperature and zero setting were not changed. Before and after each group of measurements, the 30° analyzing magnet hall probe was calibrated using the narrow resonances in ${}^7\text{Li}(\alpha, \gamma)$ at $E_\alpha=401$ and 819 keV (Be51), and γ -ray spectra of ${}^{152}\text{Eu}$ and ${}^{56}\text{Co}$ sources were accumulated for the purpose of energy calibration. One of the measurements in each group was made at $E_\alpha=819$ keV for the purpose of normalization.

Typical pressures in the target chamber during the runs were 2 to 3 torr. The measured pressures in the beam line, chamber A and chamber B were maintained below 4×10^{-6} , 2×10^{-5} and 0.02 torr respectively. Target pressure, calorimeter base temperature, analyzing-magnet current, hall probe reading, beam current and integrated charge were recorded at least once every hour. Every two hours, the accumulated γ -ray and particle spectra were written on magnetic tape, and a new particle spectrum was started.

The extended target requires that the γ -ray detector efficiency be known both as a function of γ -ray energy and position in the target. This was accomplished by moving calibrated ${}^{56}\text{Co}$, ${}^{152}\text{Eu}$ and ${}^7\text{Be}$ sources along the axis of the target chamber, accumulating spectra at 1-cm intervals.

B. Gas-cell Activity Measurement

1. Target

The gas target cell for the activation measurements is shown in figure 9. The beam is collimated with a pair of 3-mm tantalum apertures. An aluminum electron-suppression ring is connected to the beam-line and to the target cell by 2.5-cm sections of ceramic insulator. Two 4-mm copper tubes provide increased pumping to the volume downstream of the apertures. The beam enters the cell through a window consisting of a 0.66- μm nickel foil on which 0.20 μm of copper has been deposited. The purpose of the copper is to increase the thermal conductivity of the entrance foil, allowing a higher beam current. The entrance foils are attached to the foil holders with high-vacuum epoxy. The target cell is made of 0.4-mm thick stainless steel with an inside diameter of 12.7 mm. When the cell is placed on the foil holder, there is approximately 10 mm between the entrance foil and the back of the cell. A 0.025-mm platinum catcher foil was indium-soldered to the end of the target cell, and the sides of the cell were also lined with platinum foil. The cell was connected to a gas manifold (shown schematically in figure 10) by a 2-mm stainless steel tube with a section of glass insulator. The beam current was integrated in the conventional manner, by collecting the current from the electrically isolated target.

2. Detection

Prompt γ rays from the target cell were monitored with a 3 \times 3 NaI(Tl) scintillator, for the purpose of beam energy determination. The front face

of the detector was 2 cm from the center of the target cell at 90° to the beam to eliminate doppler shift.

The 100-cm³ Ge(Li) detector described in section B.2 was used to count the ⁷Be activity. During the counting, the detector was surrounded by 10 cm of lead to reduce background. The detector electronics were the same as those used for the windowless target experiment (Figure 7).

3. Experimental Procedure

The target cell was filled to ~370 torr with 99.9% ³He gas. Beams of ⁴He⁺ ions from the ONR-CIT EN tandem accelerator were used for the two activation measurements at $E_{\alpha}=2.2$ and 3.4 MeV. The beams were analyzed with a 90° double-focusing magnet stabilized by a digital NMR gaussmeter. Beam current was kept below 0.55 μ A to protect the entrance foil and to limit target heating. During the runs, the end of the target cell was cooled by a stream of air. Beam current, total charge run, NMR frequency and target pressure were recorded at least once every hour, and gas was added when the pressure fell by more than 1%. The production was continued until the estimated number of ⁷Be atoms produced exceeded 4 million.

The suppression ring was maintained at -300 volts relative to the target cell and the beam-line to prevent secondary electrons produced on the apertures from reaching the target cell. Current flow from the suppressor was monitored with an ammeter, and was always less than 1% of the total beam current on target during the production runs.

When the production was completed, the length of the target cell was measured using a depth micrometer. Additional target length from

bowing in the entrance foil caused by gas pressure was measured relative to the foil holder by using a calibrated microscope. The platinum catcher foil was then removed from the target cell and attached to a 3-mm thick lucite source holder on the front face of the Ge(Li) detector. The beam spot on the platinum catcher foil was aligned with a fiducial mark on the source holder so that it would be centered on the detector. The side and entrance foils were also counted in this manner to determine if any of the implanted beryllium had been sputtered out of the foil by the beam. The γ -ray detection efficiency was measured by counting a weak calibrated ${}^7\text{Be}$ source in this same geometry.

Beam energy loss in the entrance foil was measured by observing the energy shift in narrow (α,γ) resonances with the beam passing through the foil. For the measurement at $E_\alpha=3400$ keV, the $E_\alpha=3198$ keV (Sm62) resonance in ${}^{24}\text{Mg}(\alpha,\gamma)$ was used. A metallic magnesium target was prepared by reducing and evaporating 99.94% enriched MgO onto a 0.25-mm, oxygen-free copper blank. This target was then indium-soldered to the end of the gas cell. The 11.0 and 12.7 MeV γ -rays from this reaction were counted using a 3 \times 3-in NaI(Tl) scintillator and excitation functions for the resonance (Figure 11) were produced, first with no entrance foil, then with the entrance foil and 95, 190 and 380 Torr of ${}^3\text{He}$ gas in the cell. The effect of beam heating on the target was also studied using this resonance. At 380 torr target pressure, the shift in beam energy at resonance was measured with 150, 300, and 450 na of beam current. It was found that the 450 na beam produced a 6% decrease in effective target thickness, more than the 3% predicted on the basis of energy loss in the gas. It is believed that the additional 3% decrease is caused by local heating of the gas in the region of the entrance foil.

For the $E_{\alpha}=2400$ keV measurement, a resonance in $^{14}\text{N}(\alpha,\gamma)$ at $E_{\alpha}=2353$ keV (Ro73) was used. Since the measurement was made using a N_2 gas target, this resonance could not be observed without the entrance foil. Reaction γ rays between 2.8 and 6.5 MeV were counted and the excitation functions for target gas pressures of 160 and 340 torr, shown in figure 12, were produced.

III. DATA ANALYSIS

A. Windowless Gas Target System

The yield of γ_i from a capture reaction with cross section $\sigma_i(E)$ in an extended gas target can be written as an integral over the length of the target:

$$Y_i = \int \sigma_i(E_{cm}) f_i(E_{cm}, \theta) N_\alpha n_\tau \varepsilon(E_{\gamma_i}, z) dz . \quad (\text{III.1})$$

where:

Y_i = total yield of γ_i from the extended target

$f_i(E_{cm}, \theta)$ = angular distribution function of γ_i

N_α = total number of beam particles

n_τ = target number density

$\varepsilon(E_{\gamma_i}, z)$ = detection efficiency as a function of γ -ray energy and position.

The calculation of these five quantities and their associated errors will be discussed below. Substituting, in equation (III.1), the expression for σ_i in terms of the cross-section factor (equation I.6) gives,

$$Y_i = \int \frac{S_i(E_{cm})}{E_{cm}} e^{-2m\eta} f_i(E_{cm}, \theta) N_\alpha n_\tau \varepsilon(E_{\gamma_i}, z) dz . \quad (\text{III.2})$$

Making the assumption that the cross-section factor is constant over the range of energies in the target, the yield becomes,

$$Y_i = S_i N_\alpha n_\tau \int \frac{1}{E_{cm}} \exp \left[\frac{164.125}{\sqrt{E_{cm}}} \right] f_i(E_{cm}, \theta) \varepsilon(E_{\gamma_i}, z) dz. \quad (\text{III.3})$$

The center-of-mass energy and the γ -ray energies in equation (III.3) will be functions of position due to doppler shift and energy loss in the target:

$$E_{cm} = 0.4297 \left[E_\alpha - z \left. \frac{dE}{dx} \right|_{\text{He}} \right]$$

$$E_{\gamma_0} = \gamma(1 + \beta \cos \theta)(E_{cm} + Q_0) \quad (\text{III.4})$$

$$E_{\gamma_1} = \gamma(1 + \beta \cos \theta)(E_{cm} + Q_1)$$

$$E_{\gamma_{429}} = \gamma(1 + \beta \cos \theta)(429.2 \text{ keV}),$$

where γ and β are the relativistic parameters for the recoiling ${}^7\text{Be}$ nucleus, Q_0 and Q_1 are the Q-values for the ground-state and first excited-state radiative captures and θ is the angle to the center of the γ -ray detector. The energy loss, dE/dx , was calculated from the target density using the formulation of Ziegler (Zi77) for helium ions on helium gas.

A computer program was written to solve the integral (I_i) in equation (III.3) and to calculate the energy centroid (E_0) of the γ_0 distribution,

$$I_i = \int \frac{1}{E_{cm}} \exp \left[\frac{164.125}{\sqrt{E_{cm}}} \right] f_i(E_{cm}, \theta) \varepsilon(E_{\gamma_i}, z) dz \quad (\text{III.5})$$

and

$$E_0 = \frac{1}{I_0} \int \frac{E_{\gamma_0}}{E_{cm}} \exp \left[\frac{164.125}{\sqrt{E_{cm}}} \right] f_0(E_{cm}, \theta) \varepsilon(E_{\gamma_0}, z) dz. \quad (\text{III.6})$$

For each measurement, the incoming beam energy, E_α , was adjusted to reproduce the observed centroid, \bar{E}_{γ_0} , of the γ_0 yield. The S-factor was then calculated directly for each of the three γ -ray transitions using the formula,

$$S_i(E_t) = \frac{Y_i}{N_\alpha n_\tau I_i}, \quad (\text{III.7})$$

where E_t is the center-of-mass beam energy corresponding to the observed energy of the ground-state capture γ ray,

$$E_t = \bar{E}_{\gamma_0} - Q_0. \quad (\text{III.8})$$

The branching ratio is given by,

$$\rho_i(E_t) = \frac{Y_i I_0}{Y_0 I_i} \quad \text{for } i=1 \text{ and } 429. \quad (\text{III.9})$$

The total cross-section factor for the ${}^3\text{He}(\alpha, \gamma){}^7\text{Be}$ reaction is equal to the sum of the cross-section factors for radiative capture to the ground state (S_0) and first excited state (S_1) of ${}^7\text{Be}$. The first excited state capture cross-section factor is the weighted average of the values calculated from the yields of the two cascade γ rays, γ_1 and γ_{429} (see figure 1),

$$S_{34} = S_0 + aS_1 + bS_{429}, \quad (\text{III.10})$$

where a and b are the weighting factors,

$$a = \frac{(\Delta S_{429})^2}{(\Delta S_1)^2 + (\Delta S_{429})^2} \quad \text{and} \quad b = 1 - a. \quad (\text{III.11})$$

Similarly, the branching ratio is the weighted average of ρ_1 and ρ_{429} ,

$$\rho = \frac{\epsilon_0}{Y_0} \left[\frac{a Y_1}{\epsilon_1} + \frac{b Y_{429}}{\epsilon_{429}} \right], \quad (\text{III.12})$$

The total reaction cross section, σ_{tot} , can then be calculated from the total cross section factor using the inverse of equation (I.6).

In the following discussions of the measured parameters, the notation Δx is used to indicate the probable error in the quantity x and the notation δ_x is used for the relative error, $\delta_x \equiv \Delta x / x$.

1. γ -ray yield (Y_i)

Typical γ -ray spectra for $E_{cm}=165, 350, \text{ and } 500$ keV are shown in figure 13 with the capture γ -ray peaks (γ_0 and γ_1 and γ_{429}) indicated. Also shown are the important background γ -ray lines. The γ -ray yield (Y_i) and the statistical error (ΔY_i) for each transition was calculated by integrating the total number of counts under the peak and subtracting the number of counts below a straight-line least-squares fit to background regions above and below the peak, using the program described in detail in appendix B. This program also calculated the centroid of the γ -ray distributions, \bar{E}_{γ_0} , from which the target energy (Equation III.8) was calculated. Since the Q-value for the reaction is very accurately known, the error in the target energy (ΔE_t) was taken to be equal to the error in the γ_0 centroid ($\Delta \bar{E}_{\gamma_0}$).

2. Angular Distribution Function ($f_i(E_{cm}, \theta)$)

The theoretical angular distribution functions of Tombrello and Parker were used in these calculations. Since only the P_0 and P_2 com-

ponent have any significant value over the range of energies examined in this experiment, all other components were ignored, and the integrals in equations III.5 and III.6 were calculated using the angular distribution function

$$f_i(E_{cm}, \theta) = 1 + a_{2i}(E_{cm}) P_2(\cos \theta). \quad (\text{III.13})$$

Since the theoretical P_2 coefficient is a slowly varying function of energy, it was assumed to be a constant for each of the measurements. The values of a_{2_0} and a_{2_1} used in these calculations are shown in table 1. The γ -ray transition from the first excited state to the ground state of ${}^7\text{Be}$ is isotropic.

3. Number of Beam Particles (N_α)

The current (I_c), in microamperes, from the calorimeter controller (see appendix A) is equal to the temperature difference ($T_2 - T_1$), in Kelvins, between the beamstop and the water-cooled heatsink. The calibration constant for the calorimeter was found to be $k = 1.062 \pm 0.009$ W/K. Because of the high thermal conductivity of helium, an additional calculated quantity, 0.065 W/K must be added to this constant. The temperature difference can be converted to beam power (p) by multiplying by k . This beam power is also given by the particle energy times the beam flux in particles per second,

$$p = E_c \frac{dN_\alpha}{dt} = k(T_2 - T_1), \quad (\text{III.14})$$

where E_c is the energy of the beam at the calorimeter, calculated from the observed target energy E_t and the additional beam-energy loss in the

13.6 cm from the center of the target cell to the calorimeter beamstop

$$E_c = 2.327 E_t - 13.6 \left. \frac{dE}{dx} \right|_{He} . \quad (\text{III.15})$$

The number of beam particles is then found by integrating equation III.14,

$$N_\alpha = \frac{k}{E_c} \int (T_2 - T_1) dt = \frac{k}{E_c} \int I_c dt . \quad (\text{III.16})$$

Equation III.16 was used to convert the integrated calorimeter-controller current into the number of beam particles. The random error in N_α is given by,

$$\delta^2_{N_\alpha} = \delta^2_{E_c} + \delta^2_T + \delta^2_I, \quad (\text{III.17})$$

where, assuming a 5% error in the energy loss calculation, $(\Delta E_c)^2$ is given by

$$(\Delta E_c)^2 = (2.327 \Delta E_t)^2 + (0.05 E_{loss})^2, \quad (\text{III.18})$$

δ_T is the relative calorimeter zeroing error (1%) and δ_I is the current integration error (0.5%). In addition, the calorimeter calibration introduces a 1% systematic error in the data.

4. Target Number Density (n_τ)

The gas target density was calculated from the pressure, p , and temperature, T , of the gas which were assumed to be constant over the length of the target cell (not including the entrance canal). The pressure of the gas is measured with an aneroid pressure gauge, which was calibrated against a McLeod compound manometer. The mean pressure was

calculated from the values which were recorded hourly during the runs, and the error in the pressure, ΔP , was taken to be the calculated standard deviation of this mean pressure. The gas temperature can not be measured directly, since a radial temperature gradient exists in the target cell, but the temperature of the gas along the beam path can be estimated by assuming that all of the energy deposited in the target is conducted by the gas to the walls of the chamber, which act as an infinite, room-temperature heat sink. This assumption is reasonable, since the energy deposited was always less than 0.1 W/cm. The temperature difference (T') between two concentric cylindrical surfaces with a heat flow of H W/cm was calculated with the expression

$$T' = \frac{H}{2\pi k} \ln(b/a) \quad (\text{III.19})$$

where k is the thermal conductivity, b is the inner radius of the target chamber and a is the radius of the beam. This quantity was calculated for each run (See table 1) and added to the room temperature to give the effective target temperature, T . The decrease in target thickness as a function of energy deposition per unit length calculated in this manner agrees with the observations of Görres *et al.* (Go80), for a gas target of similar dimensions. The target density in atoms per cm^3 is then given by,

$$n_\tau = \frac{N_0}{22,400} \left(\frac{273.15}{T} \right) \left(\frac{p}{760} \right), \quad (\text{III.20})$$

where N_0 is Avogadro's number, T is in Kelvins and p is in torr. The error in n_τ is simply given by,

$$\delta^2_{n_\tau} = \delta^2_T + \delta^2_p, \quad (\text{III.21})$$

where the temperature error is assumed to be ± 4 K. The calibration of the pressure gauge introduces an additional 2% systematic error.

5. Detector Efficiency ($\varepsilon(E_\gamma, z)$)

Since the doppler broadening of γ_{429} is very small and since the γ -ray energy is independent of energy loss in the target, no energy dependence was included in the efficiency function for this transition. The integral in equation III.5 was numerically evaluated in 1-cm steps using discrete values interpolated from the detector efficiency curves measured for the 411-keV and 444-keV transitions in ^{152}Eu .

For the capture γ -rays, the calibrated source efficiency data were fitted to an empirical function of the form:

$$\varepsilon(E_\gamma, z) = \frac{a E_\gamma^b}{1 + \left[\frac{z}{c E_\gamma^d} \right]^f}. \quad (\text{III.22})$$

Figure 14 shows the measured efficiency as a function of position for several energies corresponding to γ -ray lines from the calibrated ^{56}Co and ^{152}Eu sources. Also shown in figure 14 is the best fit of equation III.22 to these data. The parameters used in this fit are given in table 2. In figure 15, the sum, over the length of the target, of the measured efficiencies was compared to a corresponding sum over the efficiency function (Equation III.22) for several γ -ray lines between 1238 and 2598 keV; approximately the range of the observed γ_0 and γ_1 transitions in this experiment. The errors shown include only the statistical error in γ -ray yield and the error in source γ -ray branching ratios. From the data in figure 15, an estimated 2% random error was assigned to the detection

efficiency. A systematic error of 3% is introduced by the γ -ray source calibrations.

6. Calculation of errors

The statistical errors in the individual cross sections were calculated from the relation,

$$\delta^2_{\sigma} = \delta^2_Y + \delta^2_{n_r} + \delta^2_{N_{\alpha}} + \delta^2_{\epsilon}. \quad (\text{III.23})$$

The errors in the total cross section and branching ratio are more complicated due to correlated errors in the weighted averages and sums. From equation (III.10) the error in the total cross section is

$$\begin{aligned} \delta^2_{\sigma_{tot}} = & \delta^2_{n_r} + \delta^2_{N_{\alpha}} + \frac{1}{\sigma_{tot}^2} \left[\sigma_0^2 (\delta^2_{Y_0} + \delta^2_{\epsilon_0}) \right. \\ & \left. + (a\sigma_1)^2 (\delta^2_{Y_1} + \delta^2_{\epsilon_0}) + (b\sigma_{429})^2 (\delta^2_{Y_{429}} + \delta^2_{\epsilon_{429}}) \right]. \end{aligned} \quad (\text{III.24})$$

Similarly, from equation (III.12), the error in the branching ratio can be written,

$$\delta^2_{\rho} = \delta^2_{Y_0} + \delta^2_{\epsilon_0} + \frac{1}{\rho^2} \left[\rho_1^2 (\delta^2_{Y_1} + \delta^2_{\epsilon_1}) + \rho_{429}^2 (\delta^2_{Y_{429}} + \delta^2_{\epsilon_{429}}) \right]. \quad (\text{III.25})$$

The error in the cross-section factors are then calculated from,

$$\delta^2_S = \delta^2_{\sigma} + \left[\delta_{E_{cm}} \left(1 - \frac{164.125}{2\sqrt{E_{cm}}} \right) \right]^2. \quad (\text{III.26})$$

A summary of the systematic errors in this measurement is given in table 3.

B. Gas-cell Activity Measurement

The gas cell activity measurement was divided into two phases; the production phase, in which the ${}^7\text{Be}$ is produced and implanted in the platinum catcher foil, and the counting phase, in which the γ rays from the β decays of the ${}^7\text{Be}$ are counted using a Ge(Li) detector. The rate of production of ${}^7\text{Be}$ atoms is given by,

$$\frac{dN_{Be}}{dt} = \int \sigma_{tot}(E_{cm}) i_{\alpha} n_{\tau} dz - \lambda N_{Be}, \quad (\text{III.27})$$

where i_{α} is the beam current in particles per second, n_{τ} is the target density and E_{cm} is a function of position due to energy loss in the gas,

$$E_{cm}(z) = 0.4297 \left[E_{\alpha} - E_{foil} - z \left. \frac{dE}{dx} \right|_{He} \right], \quad (\text{III.28})$$

and E_{foil} is the average beam-energy loss in the entrance foil.

Over the range of energies in the target, $\sigma_{tot}(E_{cm})$ is very nearly linear and is constant to within 6%, so the integral in equation (III.23) can be approximated by a constant production rate,

$$P = \int \sigma_{tot}(E_{cm}) n_{\tau} i_{\alpha} dz \approx \sigma_{tot}(E_t) N_{\tau} i_{\alpha}, \quad (\text{III.29})$$

where E_t is the center-of-mass energy at the center of the target and N_{τ} is the total gas-target thickness. For a time period of duration t , with constant current i_{α} and target density n_{τ} , the number of ${}^7\text{Be}$ atoms produced will be

$$N_{Be} = \frac{P}{\lambda} (1 - e^{-\lambda t}). \quad (\text{III.30})$$

The production phase was divided into m time periods. For each period,

the duration (t_i), average current (i_{α_i}) and target density (n_{τ_i}) were calculated from the time, charge and pressure which were recorded approximately every hour during production. The estimated production rate (P_i) was calculated from these currents and target densities using an estimated cross section, σ_{est} . The total estimated ${}^7\text{Be}$ production at the end of the production periods is given by,

$$N_{est} = \sum_{i=1}^m \frac{P_i}{\lambda} (1 - e^{-\lambda t}) \exp \left[-\lambda \sum_{j=1}^{i-1} t_j \right]. \quad (\text{III.31})$$

The counting period begins at the end of the last run ($t'=0$) The estimated number of ${}^7\text{Be}$ decays between t_1' and t_2' is given by,

$$d_{est} = N_{est} (e^{-\lambda t_1'} - e^{-\lambda t_2'}) \quad (\text{III.32})$$

The number of ${}^7\text{Be}$ decays during the counting period can be calculated from the yield of decay γ rays (Y_{478})

$$d_{Be} = \frac{Y_{478}}{0.104 \varepsilon} \quad (\text{III.33})$$

where ε is the detector efficiency and 0.104 is the measured decay branch to the first excited state of ${}^7\text{Li}$. The total cross section, $\sigma_{tot}(E_t)$, can then be found by multiplying the estimated cross section by the ratio of the measured decays to the estimated decays,

$$\sigma_{tot} = \sigma_{est} \frac{d_{Be}}{d_{est}}. \quad (\text{III.34})$$

The cross-section factor, $S_{34}(E_t)$, was then calculated from σ_{tot} using equation I.6.

1. γ -ray Yield (Y_{478})

The catcher-foil γ -ray spectrum for the $E_{\alpha}=3400$ keV activation measurement is shown in figure 16. The yield and probable error (ΔY_{478}) in the yield of the 478 keV γ ray were calculated using the procedure described in appendix B.

2. Beam Energy (E_t)

For the $E_{\alpha}=3400$ keV measurement, the center-of-mass beam energy was calculated from the centroid of the prompt γ -ray peak, using equation (III.8). Figure 17 shows the capture γ -ray spectrum and the ^{24}Na spectrum used to calibrate the γ -ray energy. The capture γ -ray energy and its probable error were calculated using the method described in appendix B. The γ -ray centroid, $\bar{E}_{\gamma_0}=2834\pm 10$ keV implies a beam energy of $E_t=1247\pm 10$ keV.

This beam energy was also calculated from the incident beam energy and the energy loss in the foil and the target gas. These energy losses were measured by observing the shift in beam energy of the center of a narrow resonance with the beam passing through the entrance foil. Foil thickness was then calculus of Ziegler (Zi77). For the foil used in this measurement, the observed en keV $^{24}\text{Mg}(\alpha,\gamma)^{28}\text{Si}$ resonance was 410 ± 5 keV, corresponding to a foil thickness of $0.86 \mu\text{m}$ ($0.66 \mu\text{m}$ nickel + $0.20 \mu\text{m}$ copper). This implies an energy loss of 432 ± 5 keV at the incident beam energy $E_{\alpha}=3400$ keV. Including the 50 ± 3 keV energy loss in the heli the calculated beam energy is $E_t=1255\pm 4$ keV in good agreement with the γ -ray calculation above.

At $E_\alpha=2750$ keV, only the energy-loss method was used to calculate target energy. An energy shift of 480 ± 8 keV in the 2348 keV, $^{14}\text{N}(\alpha,\gamma)^{18}\text{F}$ resonance was observed, corresponding to a foil thickness of $0.87\ \mu\text{m}$. The calculated energy loss for an incident $E_\alpha=2750$ keV beam is then 486 ± 8 keV in the entrance foil and 62 ± 3 keV in half the gas target, implying an average target energy of $E_t=947\pm 6$ keV.

3. Current Integration (i_α)

Since the beam consists of singly charged ^4He ions, the electrical current from the isolated target is equal to the beam particle current. Current flow from the secondary electron suppression ring was monitored, and amounted to less than 1% of the target current. The target current was integrated using a Brookhaven Nuclear Instruments model 1000 current digitizer, with a specified accuracy of 0.05%. Care was taken to accurately adjust the zero offset before each run, so the estimated relative error in the current is taken to be 1%.

4. Target Thickness (N_τ)

As in the windowless measurement, the target density, n_τ , was calculated from the pressure and temperature of the gas target. The effective temperature was calculated from the current dependent shift in the energy of the $^{24}\text{Mg}(\alpha,\gamma)$ resonance. The observed shift was $-6\pm 2\%$ at the resonance energy with a beam current of $0.45\pm 0.03\ \mu\text{A}$, and decreased linearly for currents of $0.30\ \mu\text{A}$ and $0.15\ \mu\text{A}$. At $E_\alpha=3400$ keV, the average current was $0.45\ \mu\text{A}$, so the effective temperature was taken to be

$$T = (1.06\pm 0.02)T_{\text{room}}, \quad (\text{III.35})$$

or 316 ± 6 K. For the $E_\alpha = 2750$ keV measurement, although the average beam current was lower, $0.33 \pm 0.03 \mu\text{A}$, the energy loss, and therefore the beam heating of the entrance foil was 10% higher, giving an effective temperature

$$T = (1.05 \pm 0.02) T_{\text{room}}, \quad (\text{III.36})$$

or 313 ± 6 K.

The total target thickness is given by

$$N_\tau = \frac{N_0}{22,400} \left(\frac{273.15}{T} \right) \left(\frac{p}{760} \right) l, \quad (\text{III.37})$$

where l is the measured target length. The pressure error was taken to be the standard deviation of the mean target pressure during production combined with the calibration error of the Wallace and Tiernan gauge. The error in the target thickness will then be

$$\delta^2_{N_\tau} = \delta^2_p + \delta^2_T + \delta^2_l. \quad (\text{III.38})$$

5. Detection Efficiency (ϵ)

A calibrated ^7Be source was counted in the same geometry as the catcher foil. The γ -ray yield from the source, Y_s , was calculated using the method described in appendix B. The counting efficiency is then given by;

$$\epsilon = \frac{Y_s}{0.104 a t}, \quad (\text{III.39})$$

where 0.104 is the probability for the β decay of ^7Be to the first excited

state of ${}^7\text{Li}$, a is the calibrated source strength in disintegrations per second and t is the counting time in seconds. The strength of a calibrated source with an original activity a_0 and a decay constant λ is

$$a = a_0 e^{-\lambda t}, \quad (\text{III.40})$$

where t is the elapsed time since the calibration. The error in this activity is

$$\delta^2_a = \delta^2_{a_0} + (\lambda t)^2 \delta^2_\lambda, \quad (\text{III.41})$$

and the random error in the detection efficiency is

$$\delta^2_\varepsilon = \delta^2_Y + \delta^2_a. \quad (\text{III.42})$$

The branching probability error is not included in this calculation since this same value was used in the original calculation of source strength.

6. Calculation of errors

Since the number of decays during production is small (about 1% of the total production) and since the counting began immediately after production, the error in λ will have no appreciable effect on the error in N_{est} , and the total cross section is approximated by;

$$\sigma_{tot} \approx \sigma_{est} \frac{Y_{478} e^{-\lambda t}}{0.104 \varepsilon N_\alpha N_\tau}, \quad (\text{III.43})$$

where N_α is the total integrated beam. The relative error in N_α is equal to the relative error in the current integration, so the relative error in the total cross section is

$$\delta^2_{\sigma_{tot}} = \delta^2_Y + \delta^2_{\epsilon} + \delta^2_{i_{\alpha}} + \delta^2_{N_T} + (0.02)^2 + (\lambda t')^2 \delta^2_{\lambda}, \quad (\text{III.44})$$

in which t' represents the elapsed time during counting and 0.02 is the relative error in the measured 10.4% decay branch (Aj74) to the first excited state in ${}^7\text{Li}$.

Values for all of the measured parameters and their probable errors are shown in table 4 for both of the gas cell activity measurements.

IV. RESULTS AND CONCLUSIONS

A. Experimental Results

Cross sections and branching ratios for the reaction ${}^3\text{He}(\alpha,\gamma){}^7\text{Be}$ were calculated using the methods described in section III.A for each of the 19 windowless target measurements. The results of these calculations are shown in table 5. The efficiency calibration was performed immediately after, and in the same geometry as measurements **C** and **D**. Since small changes in detector geometry were possible between groups of runs, the cross section and S-factor data in each of the other four groups were normalized to measurement **D** through their corresponding $E_\alpha=820$ keV measurements (**F**,**K**,**N** and **Q**). This normalization never amounted to more than 7%. Between the two high energy measurements (**T** and **U**), since the target system had been moved to another beam line, the detection efficiency was remeasured at several points using the ${}^{152}\text{Eu}$ source. This calibration showed less than 1% change in the measured efficiency, so no normalization was applied to these points. Also shown in table 5 are the results of the two gas cell activity measurements.

The absolute cross-section factor measurements for both experiments are shown graphically in figure 18 along with the results of the branching-ratio calculations from the windowless target. The results of these two experiments are in good agreement with each other and with the two-parameter fits of the Tombrello and Parker calculations to the data. The low-energy extrapolation of this fit gives an intercept of

$S_{34}(0)=0.52$ keV-b. A χ^2 analysis indicates an error for the fit of ± 0.01 keV-b. Including the systematic errors in the two experiments, shown in table 3, the best value for the low-energy intercept of the cross-section factor is

$$S_{34}(0) = 0.52 \pm 0.03 \text{ keV-b } (1-\sigma \text{ error}), \quad (\text{IV.1})$$

in good agreement with both the previous measurement of Parker and Kavanagh ($S_{34}(0)=0.47 \pm 0.05$ keV-b), and that of Nagatani, Dwarakanath and Ashery ($S_{34}(0)=0.61 \pm 0.07$ keV-b). Agreement with this second measurement is improved if the polynomial fit to the combined data which was used to obtain the extrapolated value is replaced with an independent fit of the Tombrello and Parker curve, giving an intercept of $S_{34}(0)=0.58 \pm 0.07$ keV-b.

The significant discrepancy between these measurements and the recently published result, $S_{34}(0)=0.30 \pm 0.03$ keV-b, of Kräwinkel *et al.* (Kr82) has been extensively studied and several possible sources of the disagreement have been uncovered. Because of the similarity between the experimental techniques used in the windowless, recirculating, gas-target measurements, the first impulse is to investigate the areas in which the two measurements differ. The most obvious difference between the two experiments is the method of beam-current integration. Whereas our experiment used the calorimeter described in appendix A, the Münster collaboration integrated their beams by counting the scattered particles using ruggedized, silicon surface-barrier detectors at 30° and 45° to the beam. There is considerable uncertainty associated with this method; the high beam currents and low energies require very small collimators to reduce the counting rate to a manageable level; multiple

scattering between these apertures can alter the count rate, and, at low energies, the particle peaks are in the tail of the detector noise. A study of our particle spectra showed 10% deviations from the calculated Rutherford scattering yield in spite of the fact that we used lower beam currents and larger apertures and obtained better resolution of the scattered α -particle and recoil ${}^3\text{He}$ peaks than the Münster collaboration. However, it seems unlikely that any combination of these effects could be responsible for the energy independent 40% increase in apparent beam current which would be needed to produce the observed cross sections. On the other hand, for our calorimeter to produce a 60% decrease in measured beam flux would require 0.6 W/K to be convected away from the beamstop by the target gas and would mean that our highest-current measurement had an average current of more than 100 μA , even though no more than 75 μA of beam was observed on the tantalum beam viewer upstream of the target system (figure 8). In addition, some other mechanism would be needed to produce a similar increase in measured cross section in the gas-cell activity measurements.

Perhaps the most likely source of the disagreement lies in the measurement of detection efficiency. In the Münster experiment, only a single commercially prepared ${}^{152}\text{Eu}$ source was used to calibrate the low energy detection efficiency in the windowless target. At higher energies, reaction γ rays from ${}^{14}\text{N}(p,\gamma)$ and ${}^{18}\text{O}(p,\gamma)$ were measured and normalized to the europium source at $E_\gamma=1408$ keV. In figure 5 of reference Kr82, the maximum absolute detection efficiency is plotted as a function of γ -ray energy. With an 80-cm³ Ge(Li) detector located 24 mm from the center of the beam, they measured an efficiency for detection of the 1408 keV transition from the ${}^{152}\text{Eu}$ source $\epsilon\sim 0.57\%$. In our experiment, using a 100-cm³

Ge(Li) detector at a distance of 25 mm from the beam, the peak efficiency was only $\varepsilon=0.46\%$, 20% less for a detector with a 25% larger volume. Depending on the relative geometry of the two detectors, this effect could certainly be responsible for the disagreement between the two experiments. Furthermore, in routinely checking the calibration of our commercially supplied ^{152}Eu source against several other calibrated sources in the lab (^{60}Co , ^7Be , ^{137}Cs and ^{22}Na), it was found the the actual source activity was 30% less than that quoted by the supplier, an effect which would have further lowered our measured efficiency to 0.35%, so it is not implausible that a commercially prepared source could be miscalibrated by this amount.

In 1981, a preprint was circulated reporting on a gas-cell activation experiment by Volk, Kräwinkel, Santo and Wallek (Vo81) in Münster. This short letter indicated a zero-energy S-factor intercept of $S_{34}(0)=0.61\pm 0.06$ keV-b based on a single measurement at $E_{\alpha}=1577$ keV. This preprint was later withdrawn from publication.

B. Relation to theory

Figure 18 shows the results of these experiments and the best fit of the Tombrello and Parker (To63) curve to the data. The reduced widths for the $^3\text{He} + ^4\text{He}$ cluster strength of the bound states used in these fits are $\theta_{1/2}^2=1.29$ and $\theta_{3/2}^2=1.33$. This indicates a strong, nearly equal cluster component in both the ground and first excited states of ^7Be , consistent with the picture of these states as a ^3He and ^4He in a relative p-state.

In table 6, the zero-energy intercepts of the best fits to five different theoretical curves are compared. The value $S_{34}(0)=0.523$ was adopted on

the basis of the three best fits to the Tombrello and Parker hard-core calculation, the Kim Izumoto and Nagatani (Ki81) Woods-Saxon phenomenological potential model and the Liu Kanada and Tang (Li81) resonating group method. The similarity of the curves calculated using several different models for the nuclear potential shows the validity of the extranuclear approximation in the original calculations; the capture cross section is quite insensitive to the details of the nuclear wavefunction.

C. Astrophysical Implications

The most recent theoretical calculation of solar-neutrino flux was reported by Bahcall *et al.* (Ba82). The predicted ^{37}Cl capture rate in the calculation is 7.6 ± 3.3 SNU ($3\text{-}\sigma$ error) adopting a value of 0.52 ± 0.15 keV-b ($3\text{-}\sigma$ error) for the zero-energy intercept of the $^3\text{He}(\alpha, \gamma)^7\text{Be}$ cross-section factor. The only effect this present measurement will have on this calculation is to reduce the uncertainty in the calculated flux.

APPENDIX A

In previous experiments in this lab (Na69 and Dw74) beam current integration in a windowless, recirculating, gas-target was accomplished by using a two-cup calorimeter, in which the temperature of a dummy cup was matched to that of an identical beamstop by resistive heating. The integrated beam power is then equal to the power delivered to the dummy-cup heater. These calorimeters usually suffered from low accuracy (4-6% random error), and were designed for beam power less than 6 W.

Using the principle that, over a relatively narrow range of temperatures, the heat flow in a metal rod is proportional to the temperature difference between the ends of the rod, we have designed a calorimeter which is capable of integrating up to 100-W beams. The body of the calorimeter, shown in figure 19, is turned from a single block of copper. It consists of a cylindrical beamstop (25-mm diam. by 12.5-mm long) connected by a 25-mm long by 10-mm diameter conduction rod to a large, cylindrical, water-cooled heatsink. The temperatures of the beamstop, T_2 , and the heatsink, T_1 , are measured by two Analog Devices model AD590 temperature transducers. These devices have the property that, with a potential between 5 V. and 30 V. applied across them, they pass a current in μA equal to the Kelvin temperature. With the two transducers placed in the bridge circuit as shown in figure 20, the current in μA flowing across the bridge, I , is equal to the temperature difference, ΔT , between the ends of the conduction rod, and is therefore proportional to

the beam power. The integrated number of beam particles, n , can then be found from the relation

$$n = (A / E_c) D$$

where A is the calorimeter calibration constant in W/K, E_c is the beam energy at the calorimeter, and D is the integrated calorimeter current

$$D = \int I dt = \int \Delta T dt .$$

If E_c is in eV, n will be in units of particle Coulombs, with E_c in joules, n will be the number of particles.

To determine the calibration constant, A , the calorimeter was placed at the end of a faraday cup and the electrical integration was compared with calorimetric integration. During the calibration runs, the temperature of the water-cooled base of the calorimeter was maintained at 298 ± 1 K. Beam current energy and integration times were varied during the calibration to test the linearity and repeatability of the calorimetric integration. The results of the calibration are shown in Table 6. For two of the calibration runs, the current integrators measuring the beam and calorimeter current were switched to check for calibration errors. During the final run, the beam was turned on for 100 seconds, then turned off. The calorimetric integration was continued until the current fell below $0.01 \mu\text{A}$ ($\Delta T < 0.01$ K). Figure 21 shows the beam current and ΔT as a function of time. The logarithmic decay of ΔT has a characteristic time constant of 25 seconds.

Heat loss by convection was estimated by measuring the characteristic time constant of the calorimeter in nitrogen at atmospheric pressure.

Conduction in nitrogen gas for the calorimeter geometry is calculable, and amounts to less than 1% of the copper rod conduction. The time constant of 23 seconds at this pressure shows convection losses of about 8%. Since convection losses in this cylindrical geometry and in this temperature and pressure range are approximately proportional to the square root of the pressure (Mc54), they should be negligible at pressures below 10 Torr.

APPENDIX B γ -RAY YIELD CALCULATION

Peaks in the γ -ray spectra were integrated using the interactive program TEKHIST. A multi-channel analyzer spectrum is displayed on a Tektronix graphics terminal, and the user defines the peak with three regions; one region containing the peak, and two background regions, usually on either side of the peak. A weighted, least-squares, linear fit to the background, of the form $y = a + bx$, is calculated using the formulas;

$$a = \frac{1}{d} \left(n \sum \frac{i^2}{y_i} - \sum \frac{i}{y_i} \sum i \right), \quad (\text{B.1})$$

and

$$b = \frac{1}{d} \left(\sum \frac{1}{y_i} \sum i - n \sum \frac{i}{y_i} \right), \quad (\text{B.2})$$

where

$$d = \sum \frac{1}{y_i} \sum \frac{i^2}{y_i} - \left(\sum \frac{i}{y_i} \right)^2, \quad (\text{B.3})$$

y_i is the number of counts in channel i , n is the total number of channels in both background regions and the summations are over all of the channels in both background regions. The χ^2 for the background linear fit is calculated from,

$$\chi^2 = \sum y_i - a n - b \sum i. \quad (\text{B.4})$$

The γ -ray yield is then the sum of the counts in the peak minus the interpolated background,

$$Y = \sum_{peak} (y_i - a - b i) = \sum_{peak} y_i - a n_p - b \sum_{peak} i, \quad (B.5)$$

where n_p is the number of channels in the peak region. The error, δ_Y , in the yield is given by,

$$\begin{aligned} \Delta Y = \sum_{peak} y_i + \frac{1}{d} \left[n_p^2 \sum \frac{i^2}{y_i} + I^2 \sum \frac{1}{y_i} \right] \\ + \frac{I - n_p}{d^2} \left[I \left(\frac{i}{y_i} \right)^2 \sum \frac{1}{y_i} - n_p \left(\sum \frac{1}{y_i} \right)^3 \right] \end{aligned} \quad (B.6)$$

The centroid of the peak is calculated from,

$$C = \frac{1}{Y} \left[\sum_{peak} i (y_i - a - b i) \right], \quad (B.7)$$

and the error in the centroid is approximated by,

$$\Delta C = w \frac{\Delta Y}{Y}, \quad (B.8)$$

where w is the full width at half maximum of the γ -ray peak.

REFERENCES

- Aj79 F. Ajzenberg-Selove, *Energy Levels of Light Nuclei, A=5-10*, Nuclear Physics **A320**, 1(1979).
- Ba67 A. D. Bacher, PhD. Thesis, California Institute of Technology, (1967).
- Ba63 J. N. Bahcall, William A. Fowler, I. Iben Jr. and R. L. Sears, *Astrophysical Journal* **137**, 344(1963).
- Ba64 John N. Bahcall, *Physical Review Letters* **12**, 300(1964).
- Ba68 J. N. Bahcall, N. A. Bahcall, W. A. Fowler and G. Shaviv, *Physics Letters* **26B**, 359(1968).
- Ba82 John N. Bahcall, Walter F. Huebner, Stephen H. Lubow, Peter D. Parker and Roger K. Ulrich, *Reviews of Modern Physics* **54**, (1982).
- Be51 W. E. Bennett, Paul A. Roys and B. J. Toppel, *Physical Review* **82**, 20(1951).
- Be39 H. A. Bethe, *Physical Review* **55**, 434(1939).
- Bu57 E. Margaret Burbidge, G. R. Burbidge, William A. Fowler and F. Hoyle, *Reviews of Modern Physics* **29**, 547(1957).
- Ca58 A. G. W. Cameron, *Bulletin of the American Physical Society Series II* **3**, 227(1958).
- Ch61 R. F. Christy and I. Duck, *Nuclear Physics* **24**, 89(1961).
- Cl80 B. T. Cleveland, R. Davis, Jr. and J. K. Rowley, *Proceedings of the Neutrino Mass Mini-Conference, University of Wisconsin Report* **186**, 38(1980).

- Da55 R. Davis, Jr., Physical Review **97**, 766(1955).
- Da64 R. Davis, Jr., Physical Review Letters **12**, 303(1964).
- Da68 R. Davis, Jr., D. S. Harmer and K. C. Hoffman, Physical Review Letters **20**, 1205(1968).
- Dw71 M. R. Dwarakanath and H. Winkler, Physical Review **C4**, 1532(1971).
- Dw74 M. R. Dwarakanath, Physical Review **C9**, 804(1974).
- Fo51 W. A. Fowler, Physical Review **81**, 655(1951).
- Fo58 W. A. Fowler, Astrophysics Journal, **127**, 551(1958).
- Fo72 W. A. Fowler, Nature **238**, 24(1972).
- Go80 J. Görres, K. U. Kettner, H. Kräwinkel and C. Rolfs, Nuclear Instruments and Methods **177**, 295(1980).
- Gr69 V. Gribov and B. Pontecorvo, Physics Letters **28B**, 493(1969).
- Ho59 H. D. Holmgren and R. L. Johnston, Physical Review **113**, 1556(1959).
- Ki81 B. T. Kim, T. Izumoto, K. Nagatani, Physical Review **C23**, 33(1981).
- Kr79 H. Kräwinkel, K. U. Kettner, W. E. Kieser, C. Rolfs, R. Santo, P. Schmalbrock, H. P. Trautvetter, R. E. Azuma and J. W. Hammer, *Jahresbericht 1978*, Universität Münster, p. 35(1979).
- Kr82 H. Kräwinkel, H. W. Becker, L. Buchmann, J. Görres, K. U. Kettner, W. E. Kieser, R. Santo, P. Schmalbrock, H. P. Trautvetter, A. Vlieks, C. Rolfs, J. W. Hammer, R. E. Azuma and W. S. Rodney, Zeitschrift für Physik **A304**, 307(1982).
- Li69 L. Marshall Libbey and F. J. Thomas, Nature **222**, 1238(1969).
- Li81 Q. K. K. Liu, H. Kanada and Y. C. Tang, Physical Review **C23**, 645(1981).

- Mc54 W. H. McAdams, *Heat Transmission*, McGraw-Hill, New York, p.176(1954).
- Na69 K. Nagatani, M. R. Dwarakanath and D. Ashery, Nuclear Physics **A128**, 325(1969).
- Pa63 P. D. Parker and R. W. Kavanagh, Physical Review **131**, 2578(1963).
- Pa66 P. D. Parker, Physical Review **150**, 851(1966).
- Ro73 C. Rolfs, A. M. Charlesworth and R. E. Azuma, Nuclear Physics **A199**, 257(1973).
- Ro80 Claus Rolfs, *Proceedings of The 1980 International Summer School on Nuclear Structure*, to be published.
- Sa68 S. Saito, Progress of Theoretical Physics **40**, 893(1968).
- Sa52 Edwin E. Salpeter, Physical Review **88**,547(1952).
- Sm62 P. J. M. Smulders and P. M. Endt, Physica **28**, 1093(1962).
- To61 T. A. Tombrello and G. C. Phillips, Physical Review **122**, 224(1961).
- To63 T. A. Tombrello and P. D. Parker, Physical Review **131**, 2582(1963).
- Tr81 H. P. Trautvetter, Comments on Nuclear and Particle Physics **10**, 123(1981).
- Vo81 H. Volk, H. Kräwinkel, R. Santo and L. Wallek, preprint, unpublished.
- Wi81 R. D. Williams and S. E. Koonin, Physical Review **C23**, 2773(1981).
- Zi77 J. F. Ziegler, *Helium: Stopping Power and Ranges in All Elemental Matter*, Pergamon Press, New York(1977).

TABLE 1
WINDOWLESS TARGET RUN PARAMETERS

The table on the next two pages shows the run parameters for each of the individual windowless target measurements. The groups of measurements described in section II.A.3 are separated by single horizontal lines. Four of the runs were not used in the final calculations, for the reasons given in the footnotes. In this and all of the following tables, the small italic numbers represent the probable error in the last digit of the preceding number (*e.g.* 1757.5 *19* means 1757.5 ± 1.9).

TABLE 1
WINDOWLESS TARGET RUN PARAMETERS

Run	E_{α} keV	E_t keV	E_{γ_0} keV	I_{α} μA
A*	407 <i>s</i>	171.1	1757.5 <i>19</i>	20
B*	830 <i>s</i>	355.7	1942.1 <i>12</i>	30
C	406 <i>s</i>	166.6	1753.0 <i>13</i>	28
D	826 <i>z</i>	346.6	1933.1 <i>9</i>	33
E	515 <i>s</i>	212.7	1799.1 <i>10</i>	22
F	820 <i>z</i>	343.6	1930.0 <i>8</i>	33
G	669 <i>z</i>	279.5	1865.9 <i>8</i>	38
H	1069 <i>s</i>	450.9	2037.3 <i>13</i>	23
I	458 <i>s</i>	192.4	1778.8 <i>22</i>	31
J	469 <i>s</i>	193.5	1779.9 <i>12</i>	41
K	818 <i>z</i>	342.9	1929.3 <i>9</i>	61
L	820 <i>z</i>	343.7	1930.1 <i>12</i>	40
M	1172 <i>s</i>	496.1	2082.5 <i>12</i>	46
N	817 <i>s</i>	342.6	1929.0 <i>12</i>	48
O	404 <i>s</i>	165.5	1751.9 <i>21</i>	33
P	404 <i>s</i>	165.8	1752.2 <i>11</i>	45
Q	804 <i>s</i>	336.7	1923.0 <i>9</i>	40
R	1152 <i>s</i>	486.1	2073.5 <i>11</i>	24
S	1036 <i>s</i>	437.0	2023.4 <i>12</i>	32
T	1200 <i>z</i>	507.4	2093.8 <i>8</i>	25
U	2735 <i>12</i>	1169.0	2755.4 <i>51</i>	1

* Preliminary investigation using 60 cm³ Ge(Li) detector. Detection efficiency was not measured with this detector.

TABLE 1 (cont.)
WINDOWLESS TARGET RUN PARAMETERS

Run	Charge C.	p torr	ΔT K	a_{20}	a_{21}
A	6.10 <i>7</i>	2.48 <i>9</i>	5.8	-0.08	-0.10
B	1.31 <i>2</i>	2.58 <i>10</i>	9.9	-0.02	-0.03
C	6.426 <i>83</i>	2.72 <i>9</i>	8.9	-0.08	-0.10
D	1.349 <i>14</i>	2.67 <i>11</i>	11.3	-0.02	-0.03
E	3.396 <i>38</i>	2.73 <i>8</i>	7.6	-0.07	-0.08
F	1.150 <i>12</i>	2.74 <i>5</i>	11.5	-0.02	-0.03
G	2.143 <i>22</i>	2.56 <i>8</i>	12.6	-0.04	-0.06
H	0.263 <i>3</i>	2.89 <i>3</i>	8.0	0.01	-0.01
I	3.708 <i>57</i>	1.35 <i>15</i>	5.2	-0.07	-0.09
J	4.920 <i>59</i>	2.72 <i>4</i>	13.6	-0.07	-0.09
K	1.450 <i>16</i>	2.86 <i>3</i>	22.2	-0.02	-0.03
L	0.694 <i>8†</i>	2.67 <i>3</i>	13.6	-0.02	-0.03
M	0.476 <i>5</i>	2.62 <i>4</i>	14.2	0.03	0.01
N	0.696 <i>7</i>	2.73 <i>10</i>	16.6	-0.02	-0.03
O	2.311 <i>37‡</i>	2.75 <i>6</i>	10.8	-0.08	-0.10
P	9.98 <i>12</i>	2.78 <i>4</i>	14.8	-0.08	0.10
Q	1.330 <i>14</i>	2.75 <i>3</i>	14.1	-0.02	-0.03
R	0.728 <i>8</i>	2.69 <i>4</i>	7.5	0.02	0.01
S	0.611 <i>7</i>	2.80 <i>3</i>	10.7	0.01	-0.01
T	1.049 <i>11</i>	2.90 <i>3</i>	8.4	0.03	0.01
U	0.0504 <i>6</i>	3.30 <i>5</i>	0.2	0.09	0.09

† Calorimeter cooling temporarily off.

‡ Run aborted due to calorimeter zero offset.

TABLE 2
EMPIRICAL EFFICIENCY FUNCTION

The data for the detection efficiency in the windowless target were fitted with a function of the form:

$$\varepsilon(E, z) = \frac{a E^b}{1 + \left[\frac{z}{c E^d} \right]^f},$$

where the constants a , b , c , d and f for the best fit are given in the table below.

constant	value
a	2.004
b	-0.833
c	1.6672
d	0.08899
f	2.40

TABLE 3
SYSTEMATIC ERRORS

A summary of the systematic errors in the windowless target system and the gas-cell activity measurements is shown in this table.

TABLE 3
SYSTEMATIC ERRORS

Windowless Target		
Variable	error	Source
Beam current	1%	Calorimeter calibration
	3%	Conduction and convection loss
Target pressure	2%	Pressure gauge calibration
Detection efficiency	3%	Source calibration
	2%	Efficiency fit
TOTAL	5.3%	

Gas-cell Target		
Variable	error	Source
Current Integration	0.5%	Integration error
Pressure	1%	Pressure gauge calibration
Detection efficiency	3%	Source calibration
TOTAL	3.3%	

TABLE 4
ACTIVITY MEASUREMENT RUN PARAMETERS

This table shows the run parameters for the two gas-cell activity measurements.

TABLE 4
ACTIVITY MEASUREMENT PARAMETERS

Parameter	V	W
E_{α} (keV)	3400	2750
p (torr)	368 <i>s</i>	368 <i>s</i>
T (K)	316 <i>s</i>	313 <i>s</i>
l (mm)	9.56 <i>10</i>	9.39 <i>10</i>
E_{loss} (keV)		
foil	432 <i>s</i>	486 <i>s</i>
He gas	92 <i>s</i>	117 <i>s</i>
E_t (keV)	1255 <i>4</i>	947 <i>s</i>
Charge (mC)	30.36	22.31
ϵ (%)	5.76 <i>10</i>	5.65 <i>10</i>
Y_{478}	2227 <i>88</i>	2097 <i>93</i>
Count time (h)	144	240

TABLE 5
RESULTS

The table on the following two pages shows the results of both experiments. The normalization of each group to run **D** has not been applied to these data. The normalized data are plotted in figure 18.

**TABLE 5
RESULTS**

Run	E_t (keV)	γ -ray yields		
		Y_0	Y_1	Y_{429}
A	171.1 <i>19</i>	490 <i>31</i>	310 <i>37</i>	682 <i>46</i>
B	355.7 <i>12</i>	1917 <i>45</i>	1029 <i>43</i>	2759 <i>60</i>
C	166.6 <i>13</i>	826 <i>37</i>	393 <i>43</i>	632 <i>48</i>
D	346.6 <i>9</i>	2719 <i>54</i>	1245 <i>49</i>	2644 <i>61</i>
E	212.7 <i>10</i>	1196 <i>40</i>	611 <i>39</i>	1154 <i>49</i>
F	343.6 <i>8</i>	2424 <i>51</i>	1167 <i>45</i>	2409 <i>58</i>
G	279.5 <i>8</i>	2244 <i>50</i>	1147 <i>50</i>	2126 <i>54</i>
H	450.9 <i>13</i>	1317 <i>38</i>	713 <i>36</i>	1409 <i>43</i>
I	192.4 <i>22</i>	389 <i>25</i>	178 <i>25</i>	367 <i>37</i>
J	193.5 <i>12</i>	996 <i>36</i>	490 <i>34</i>	948 <i>44</i>
K	342.9 <i>9</i>	2697 <i>54</i>	1409 <i>50</i>	2831 <i>60</i>
L	343.7 <i>12</i>	1539 <i>41</i>	766 <i>36</i>	1588 <i>46</i>
M	496.1 <i>12</i>	2398 <i>51</i>	1095 <i>46</i>	2659 <i>59</i>
N	342.6 <i>12</i>	1346 <i>38</i>	699 <i>35</i>	1414 <i>43</i>
O	165.5 <i>21</i>	245 <i>20</i>	93 <i>18</i>	160 <i>23</i>
P	165.8 <i>12</i>	965 <i>39</i>	467 <i>46</i>	869 <i>47</i>
Q	336.7 <i>9</i>	2468 <i>51</i>	1067 <i>45</i>	2321 <i>45</i>
R	486.1 <i>11</i>	3304 <i>60</i>	1570 <i>57</i>	3652 <i>71</i>
S	437.0 <i>12</i>	2182 <i>48</i>	1133 <i>46</i>	2375 <i>56</i>
T	507.4 <i>8</i>	6651 <i>84</i>	3173 <i>80</i>	7210 <i>98</i>
U	1169.0 <i>52</i>	1091 <i>44</i>	512 <i>51</i>	1703 <i>93</i>
V	1255. <i>4</i>			
W	947. <i>5</i>			

TABLE 5 (cont.)
RESULTS

Run	S_0 keV-b	S_1 keV-b	S_{34} keV-b	σ_{tot} nb	ρ σ_1/σ_0
A	*	*	*	*	*
B	*	*	*	*	*
C	0.393 <i>29</i>	0.144 <i>11</i>	0.536 <i>38</i>	7.70	0.365 <i>31</i>
D	0.294 <i>16</i>	0.116 <i>5</i>	0.410 <i>20</i>	175	0.394 <i>15</i>
E	0.324 <i>18</i>	0.139 <i>7</i>	0.463 <i>23</i>	28.2	0.428 <i>24</i>
F	0.311 <i>16</i>	0.127 <i>5</i>	0.438 <i>20</i>	182	0.408 <i>16</i>
G	0.339 <i>16</i>	0.140 <i>6</i>	0.479 <i>20</i>	93.6	0.414 <i>16</i>
H	0.309 <i>13</i>	0.134 <i>5</i>	0.443 <i>14</i>	432	0.434 <i>20</i>
I	0.308 <i>44</i>	0.123 <i>21</i>	0.431 <i>60</i>	16.2	0.399 <i>44</i>
J	0.295 <i>17</i>	0.124 <i>7</i>	0.419 <i>20</i>	16.3	0.421 <i>25</i>
K	0.271 <i>10</i>	0.119 <i>4</i>	0.390 <i>11</i>	161	0.439 <i>16</i>
L	0.323 <i>13</i>	0.137 <i>4</i>	0.460 <i>14</i>	192	0.425 <i>19</i>
M	0.277 <i>11</i>	0.115 <i>5</i>	0.392 <i>12</i>	497	0.414 <i>16</i>
N	0.292 <i>16</i>	0.125 <i>6</i>	0.417 <i>20</i>	171	0.417 <i>20</i>
O	0.334 <i>38</i>	0.101 <i>15</i>	0.435 <i>46</i>	7.57	0.304 <i>46</i>
P	0.303 <i>19</i>	0.123 <i>8</i>	0.426 <i>23</i>	7.49	0.406 <i>27</i>
Q	0.292 <i>11</i>	0.112 <i>4</i>	0.404 <i>12</i>	156	0.404 <i>12</i>
R	0.247 <i>9</i>	0.104 <i>4</i>	0.351 <i>10</i>	421	0.420 <i>15</i>
S	0.250 <i>9</i>	0.109 <i>4</i>	0.359 <i>10</i>	320	0.435 <i>17</i>
T	0.291 <i>9</i>	0.120 <i>3</i>	0.411 <i>11</i>	554	0.411 <i>12</i>
U	0.210 <i>11</i>	0.095 <i>5</i>	0.305 <i>14</i>	2150	0.454 <i>32</i>
V			0.304 <i>16</i>	2340	
W			0.364 <i>24</i>	1850	

* Detection efficiency was not measured for these runs.

TABLE 6
THEORETICAL FITS

The fits of several different theoretical calculations to the present cross-section factor data are compared in this table. The χ^2 for each of the fits and the zero-energy intercept of the cross-section factor are tabulated. Also shown is the χ^2 and the zero-energy intercept for the best quadratic fit to the experimental data.

TABLE 6
THEORETICAL FITS

Reference	$S_{34}(0)$	χ^2
To63	0.522 <i>11</i>	24.1
Ki81		
Hard core	0.533 <i>11</i>	27.9
Woods-Saxon	0.518 <i>10</i>	24.3
OCM	0.532 <i>10</i>	26.2
Li81	0.522 <i>10</i>	24.2
Quadratic fit	0.523 <i>10</i>	24.0

TABLE 7
CALORIMETER CALIBRATION

The calorimeter calibration measurements are shown in this table. The beam current and calorimeter current were integrated using two different current digitizers. For two of the measurements, these two digitizers were exchanged. The calibration constant is calculated from

$$A = \frac{nE_c}{D}$$

where n is in mC, E_c is in keV and D , the integrated temperature difference, is in Kelvin-seconds.

TABLE 7.
CALORIMETER CALIBRATION

E_α MeV	I_α μA	n mC	D K-sec	D/E	A w/K
0.819	14	1.996	1.519	1.855	1.076
0.819	35	3.000	2.320	2.833	1.059
0.819	35	3.000	2.293	2.800	1.071
0.819	35	3.000	2.292	2.799	1.072
0.819	7	1.000	0.7716	0.9421	1.061
0.819	7	1.000	0.7709	0.9412	1.062
0.819	4	1.000	0.7592	0.9270	1.079
0.401	15	1.000	0.3748	0.9346	1.070
0.401	15	1.000	0.3796	0.9465	1.057
0.401	15	1.000	0.3777	0.9419	1.062
0.401	30	3.000	1.1382	2.838	1.057
0.401	30	3.000	1.1491	2.865	1.047
0.401	30	3.000	1.1461	2.858	1.050
0.401	30	2.641*	1.000	2.494	1.059
0.401	30	13.228*	5.034	13.227	1.054
0.401	32†	3.444	1.299	3.239	1.063
avg.					1.062 γ

* charge and calorimeter integrators switched

† interrupted beam

FIGURE 1
ENERGY LEVEL DIAGRAM

This diagram shows the energy levels and Q-values for the reaction ${}^3\text{He}(\alpha, \gamma){}^7\text{Be}$ reaction, and for the subsequent decay of the ${}^7\text{Be}$. The γ rays (γ_0 , γ_1 , γ_{429} and γ_{478}) referred to in the text are shown. The energy levels and β -decay branching ratios are taken from Ajzenberg-Selove (Aj79).

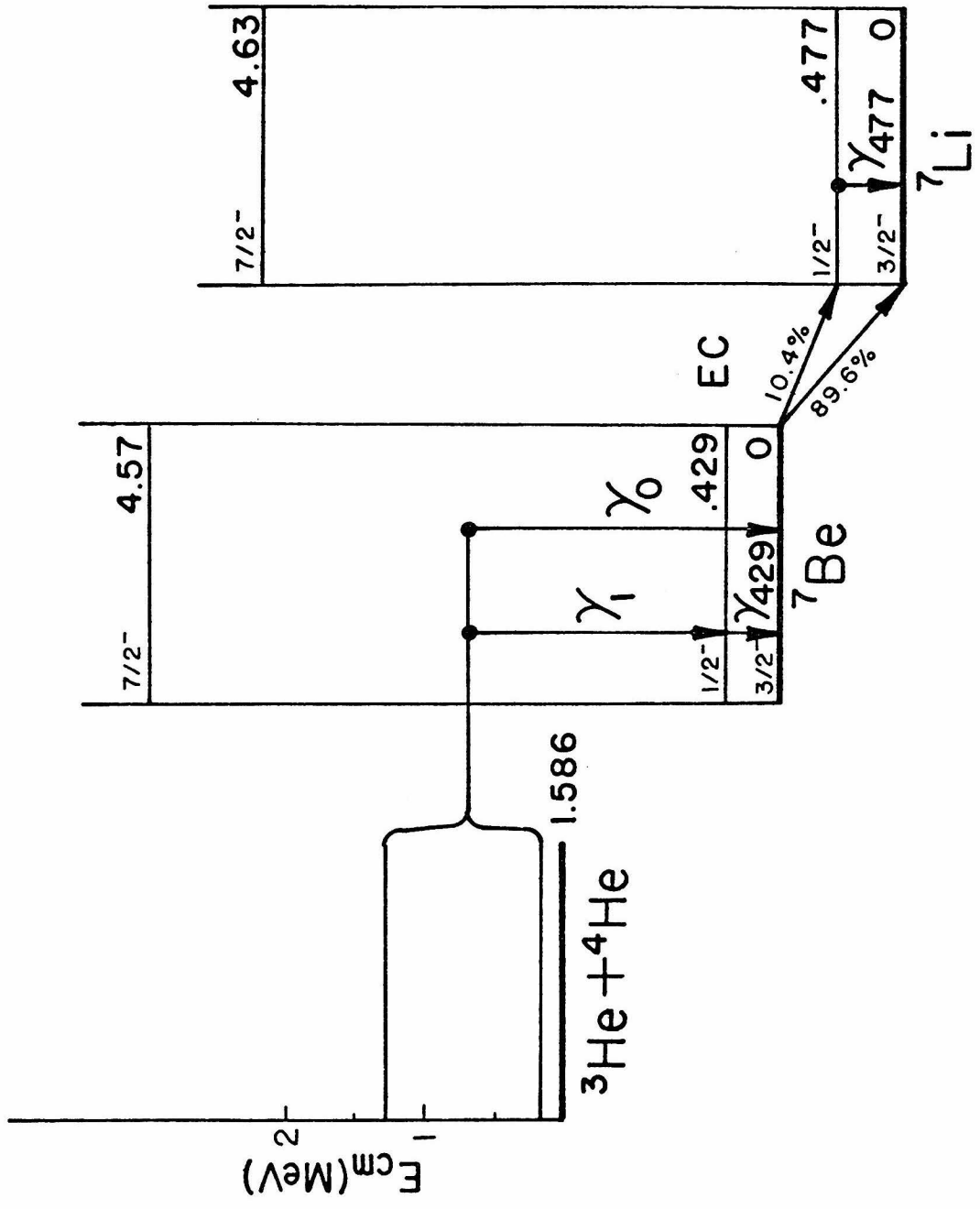


FIGURE 2
RESULTS OF PREVIOUS EXPERIMENTS

The experimental cross-section factor and branching ratio data of Parker and Kavanagh (Pa63) and Nagatani, Dwarakanath and Ashery (Na69) are indicated by the square and triangular data points respectively. The solid line shown is the best fit of the Tombrello and Parker (To63) curves to the data of Parker and Kavanagh, using the reduced widths $\theta_{3/2}^2=1.25$ and $\theta_{1/2}^2=1.05$.

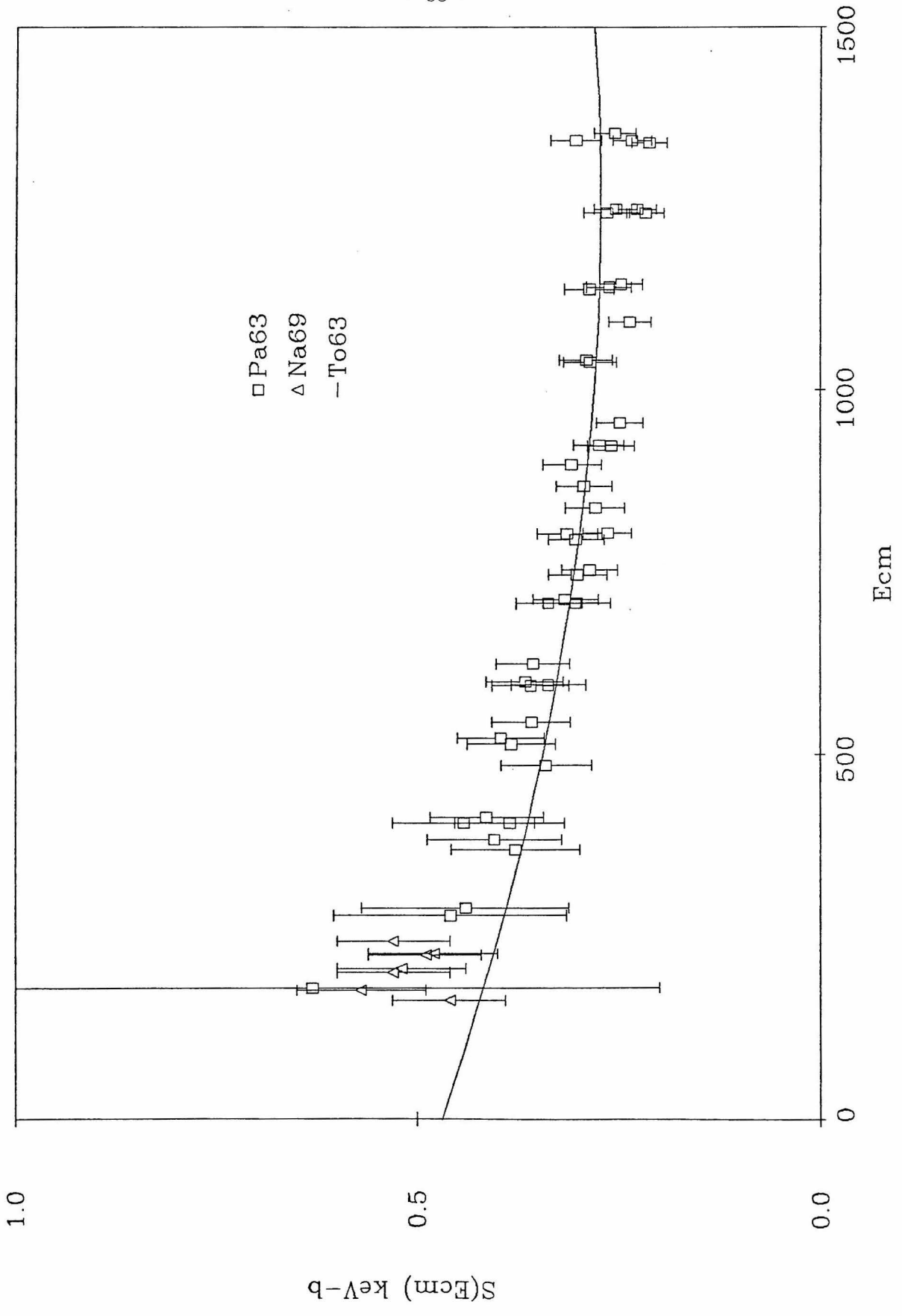


FIGURE 3
THEORETICAL CALCULATIONS

The theoretical calculations of the cross-section factor and branching ratio by Tombrello and Parker (To63), Liu, Kanada and Tang (Li81) and the three different calculations of Kim, Izumoto and Nagatani (Ki81) using a hard core potential (H-C), a Woods-Saxon potential (W-S) and the orthogonality condition model (OCM) are compared.

FIGURE 4
WINDOWLESS, DIFFERENTIALLY PUMPED, GAS-TARGET SYSTEM

This figure is a schematic representation of the gas pumping, recirculating and purifying system for the windowless target. The canals, chambers, and apertures are described in detail in section II.A.1.

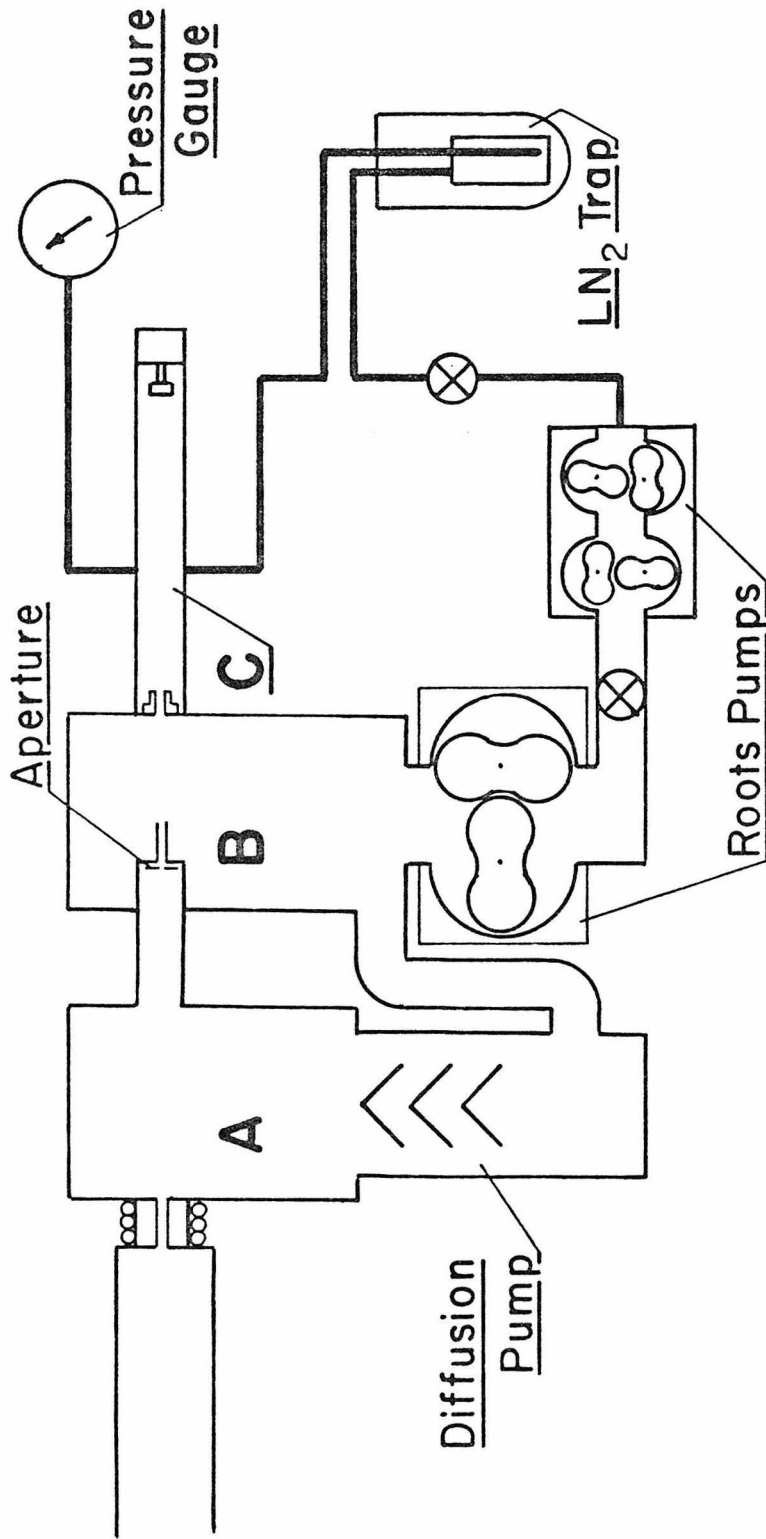


FIGURE 5
WINDOWLESS TARGET

The windowless gas target is shown from the entrance canal to the calorimeter. During the runs, the target chamber and the Ge(Li) detector were surrounded with 10 cm of lead shielding to reduce γ -ray background.

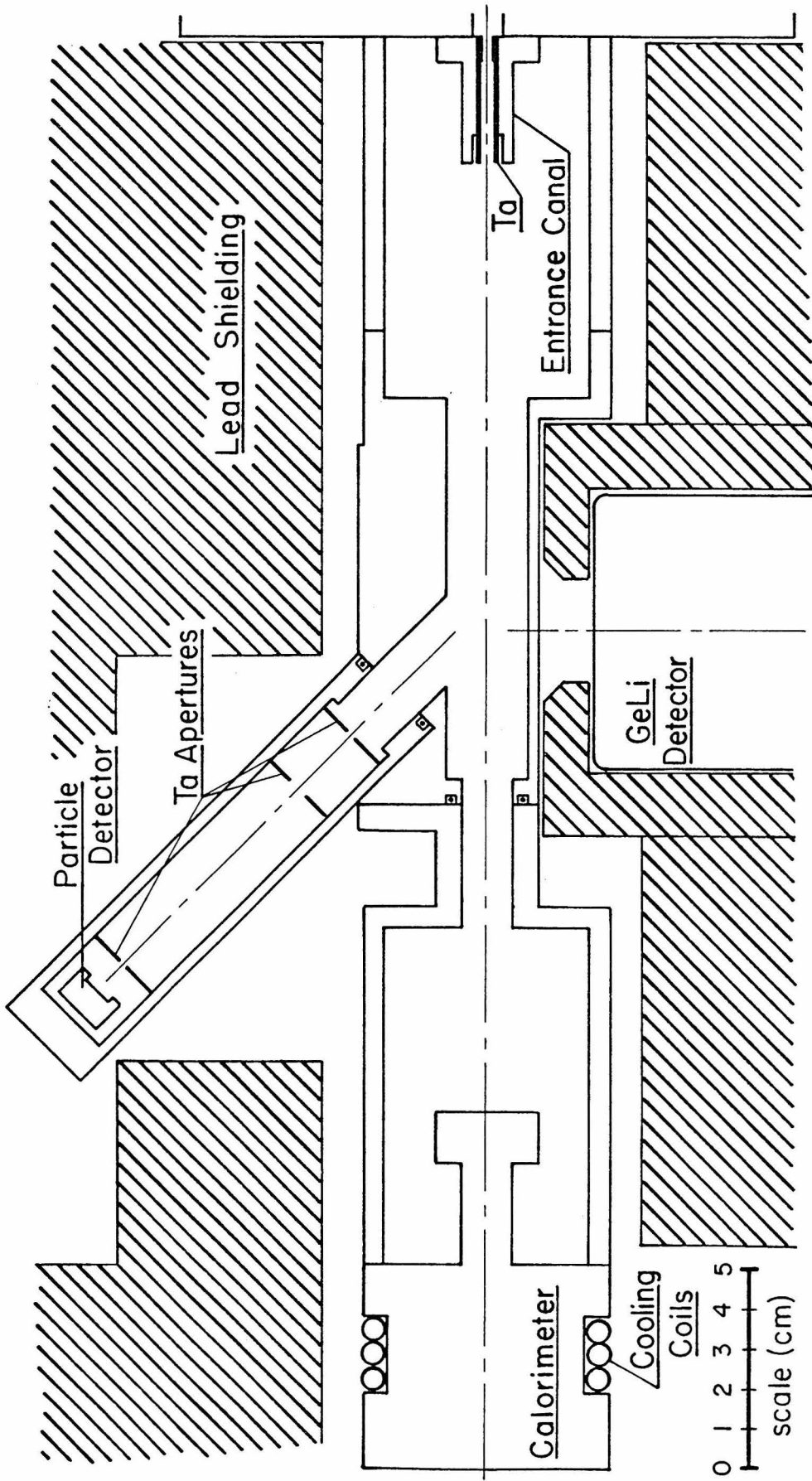


FIGURE 6
PARTICLE SPECTRA

Two typical particle detector spectra for $E_{cm}=166$ and 347 keV are shown. The 165 keV spectrum represents 0.31 particle coulombs of beam, while the 350 keV spectrum was acquired for 0.29 particle coulombs. The indicated peak positions are:

- a: Scattered ^4He
- b: Recoil ^3He
- c: ^4He scattered from ^{14}N
- d: ^4He scattered from ^{40}Ar

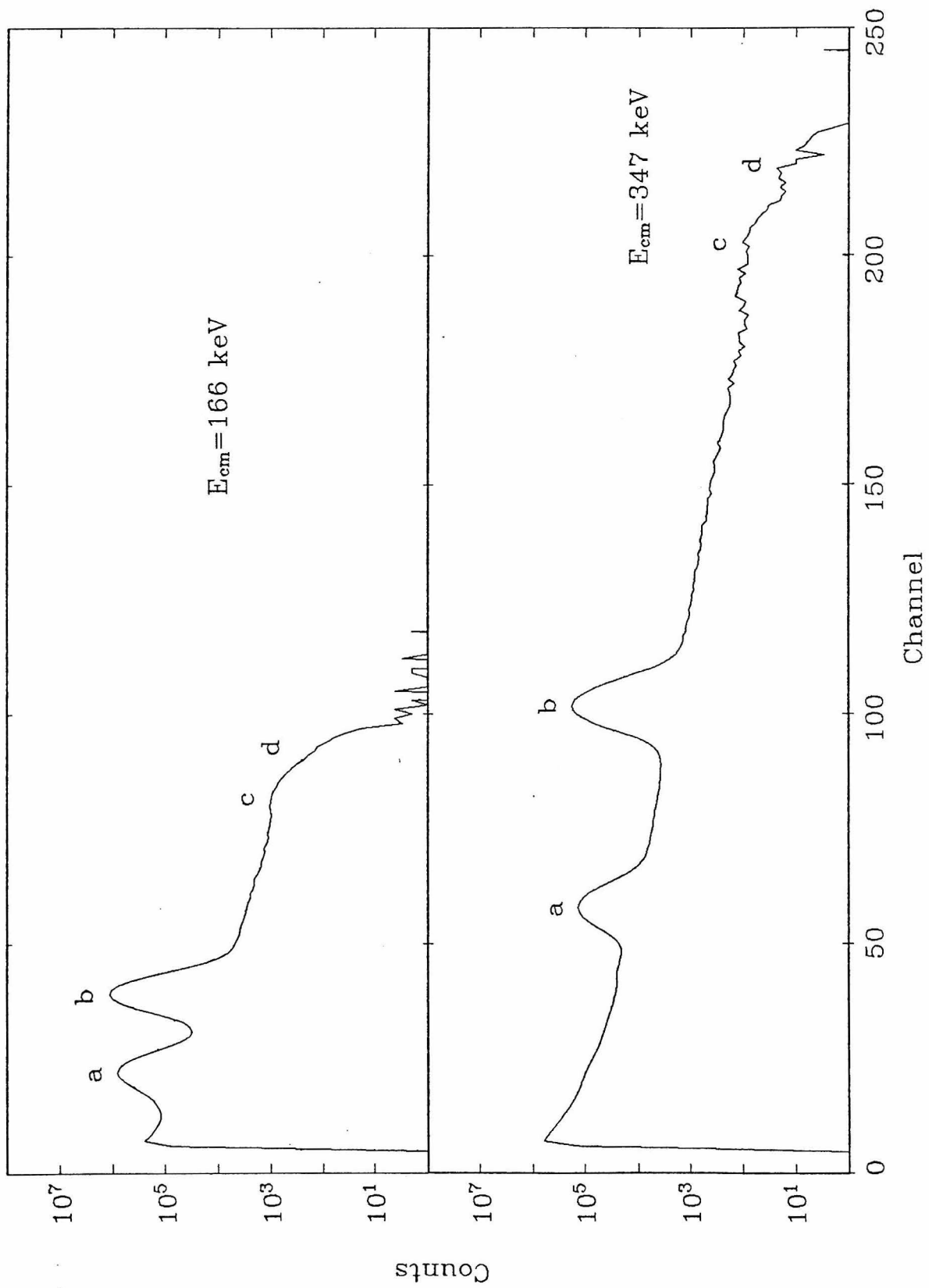


FIGURE 7
DETECTOR ELECTRONICS

The electronics for the particle detector and the lithium-drifted germanium (Ge(Li)) γ -ray detector used in the windowless-target measurements are shown in this block diagram. The gain of the γ -ray detector was adjusted to give approximately 1 keV per channel into 4096 channels. The same electronics were used for the counting phase of the gas-cell activity measurements, except that only 1024 channel spectra were used.

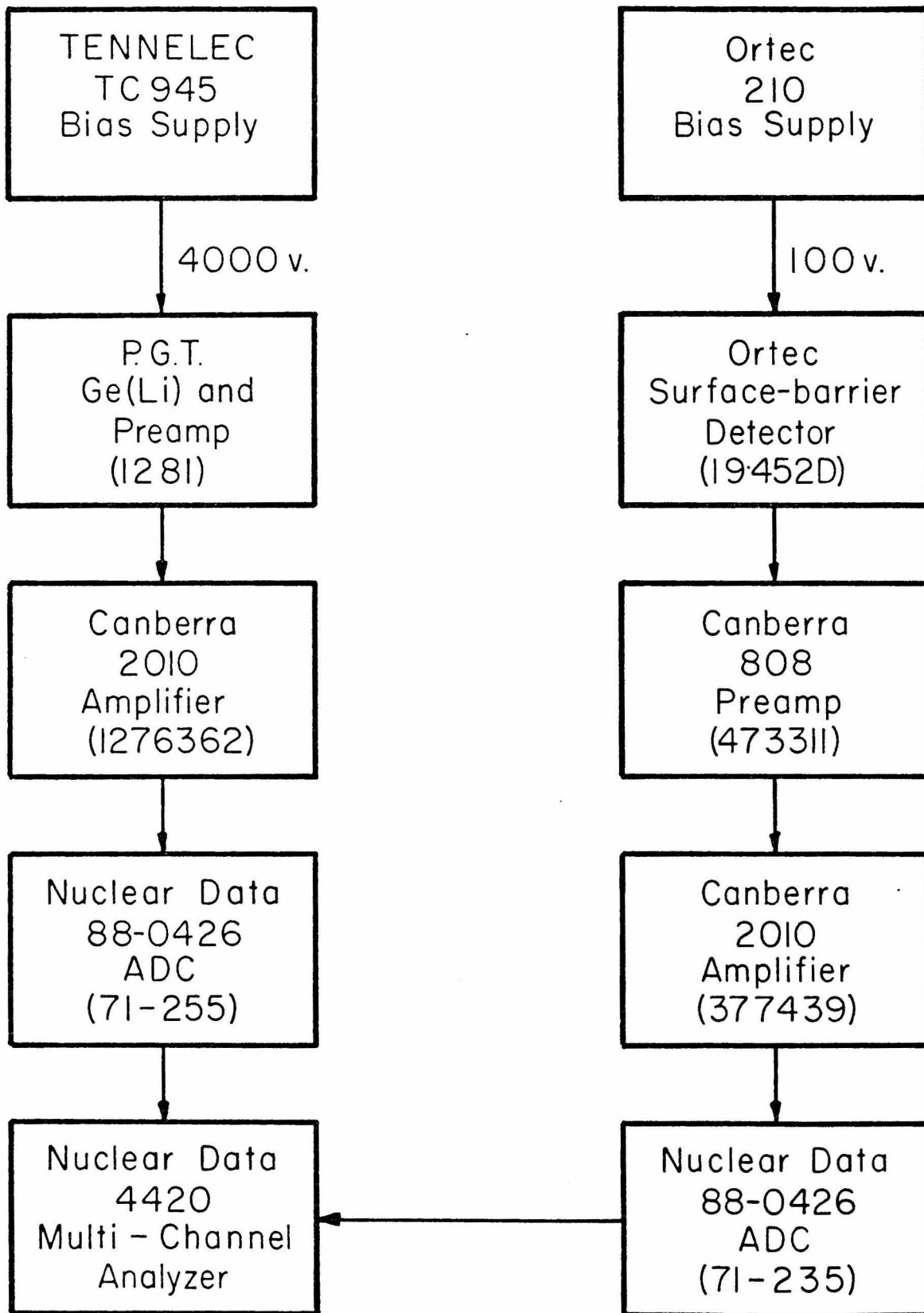


FIGURE 8
WINDOWLESS TARGET BEAMLINER

A scale drawing of the accelerator, beamline, optics, pumping and energy regulation systems constructed for the low-energy, windowless-target measurements is shown. Current from the regulating slits was fed-back to the JN accelerator Corona control system to stabilize the terminal voltage.

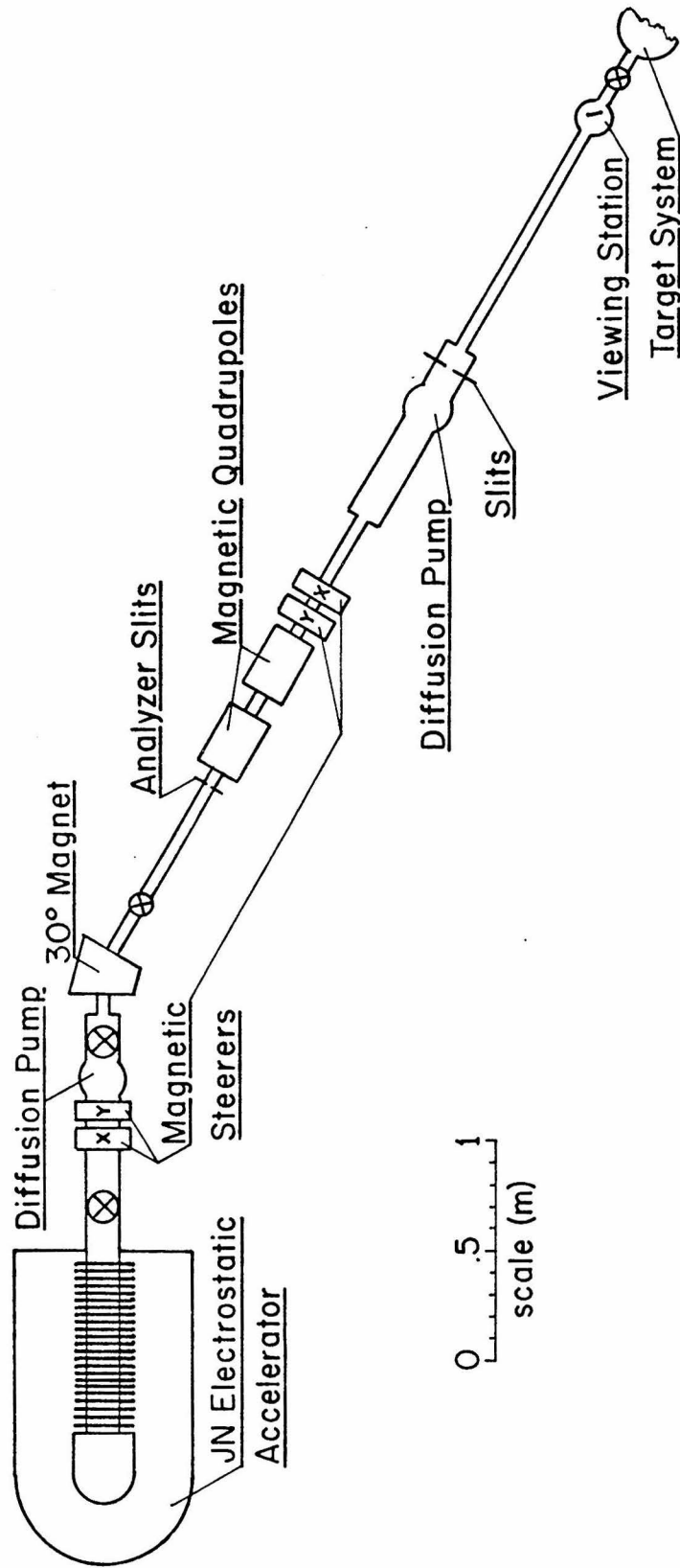


FIGURE 9
GAS CELL

This drawing shows the gas-cell target used in the activity measurements.

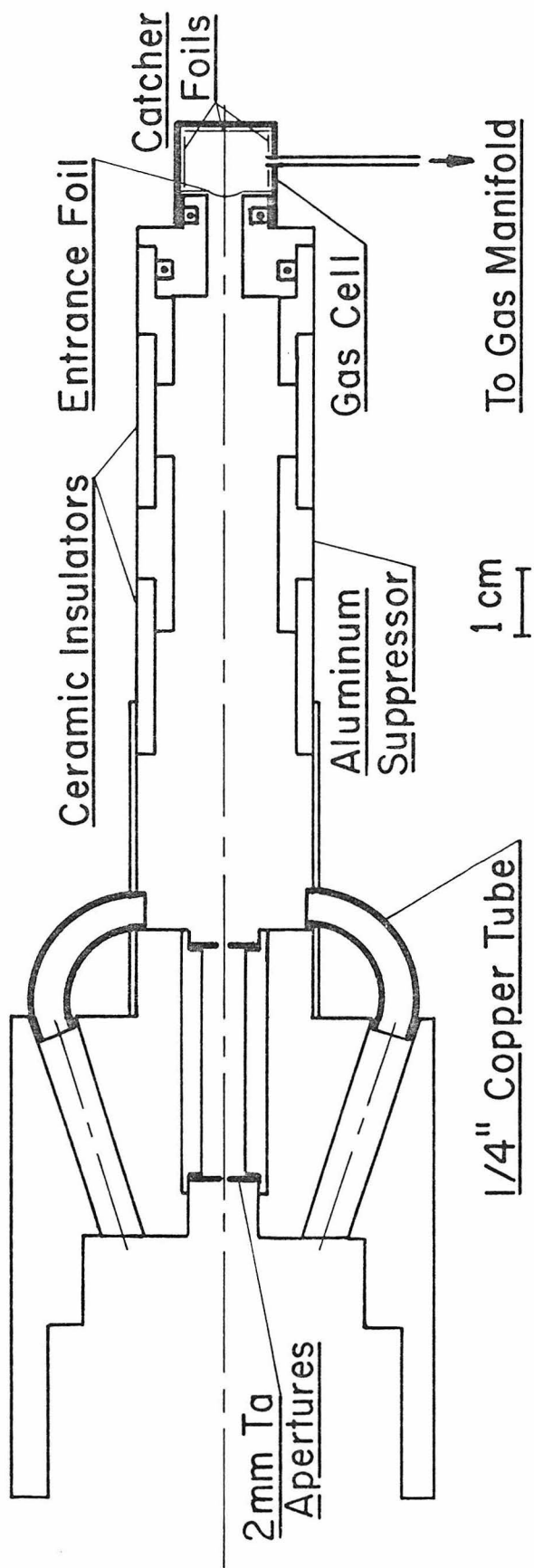


FIGURE 10
TARGET CELL GAS MANIFOLD

This figure depicts the gas manifold used with the gas-target cell shown in figure 9. For the two measurements, the cell was evacuated to below 0.02 torr and filled from a bottle containing 99.99% ^3He gas. In the foil thickness measurement using the $^{14}\text{N}(\alpha,\gamma)$ resonance, dry N_2 gas was substituted.

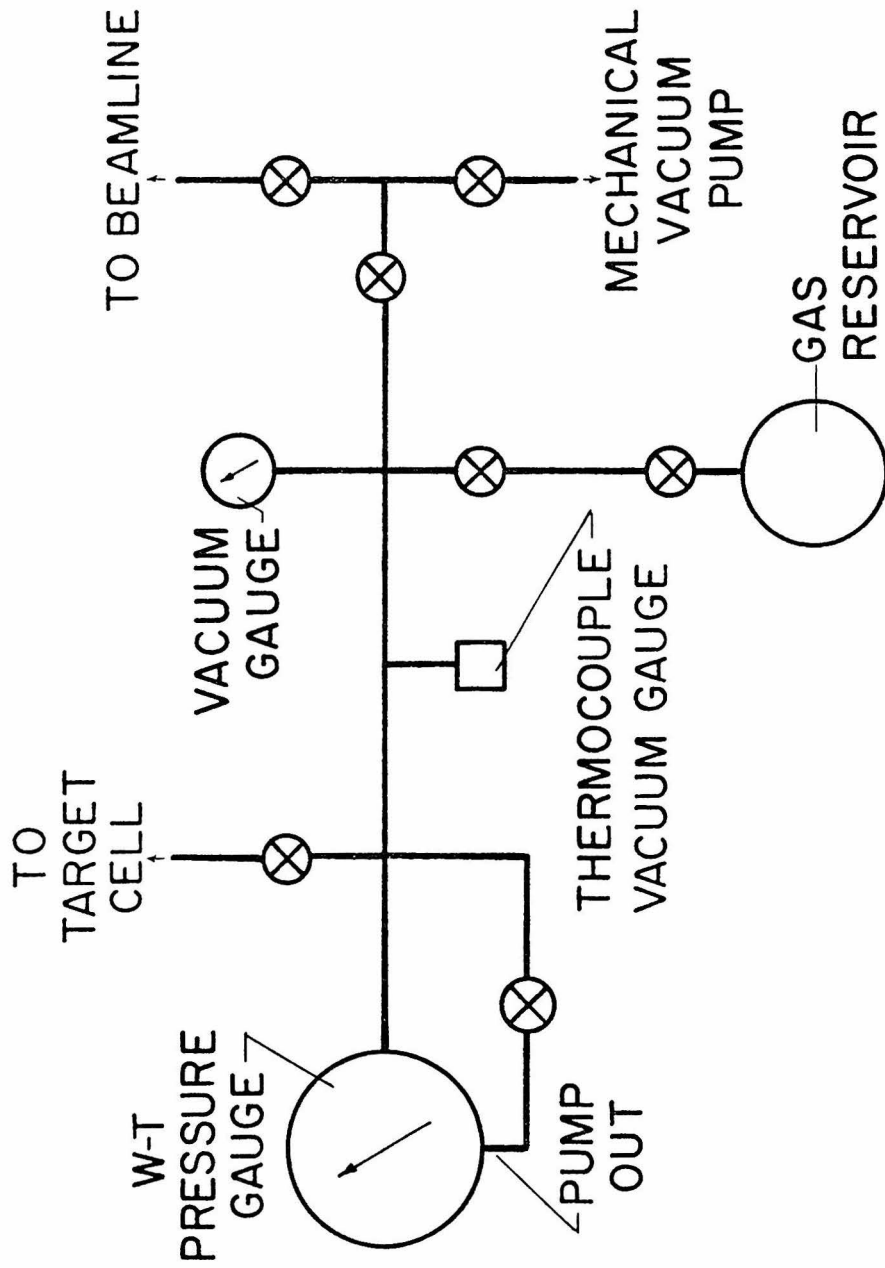


FIGURE 11

$^{24}\text{Mg}(\alpha,\gamma)^{28}\text{Si}$ FOIL THICKNESS MEASUREMENTS

These curves show the excitation functions for the reaction $^{24}\text{Mg}(\alpha,\gamma)^{28}\text{Si}$ with an α beam on a metallic magnesium target. Curve A is with no foil in the beam. Curves B, C and D were taken with the entrance foil and 90, 180 and 360 torr of ^3He gas in the target cell respectively. The square points represent the excitation function of the resonance at 3198 keV. The diamonds, triangles, and bars represent the excitation function with the beam passing through the entrance foil and the target cell filled with 90, 180, and 360 torr of ^3He gas respectively. Extrapolation to zero pressure yields a foil thickness of 432 ± 5 keV. The additional loss in the gas at 360 torr with $0.15 \mu\text{A}$ of beam current is 96 ± 5 keV.

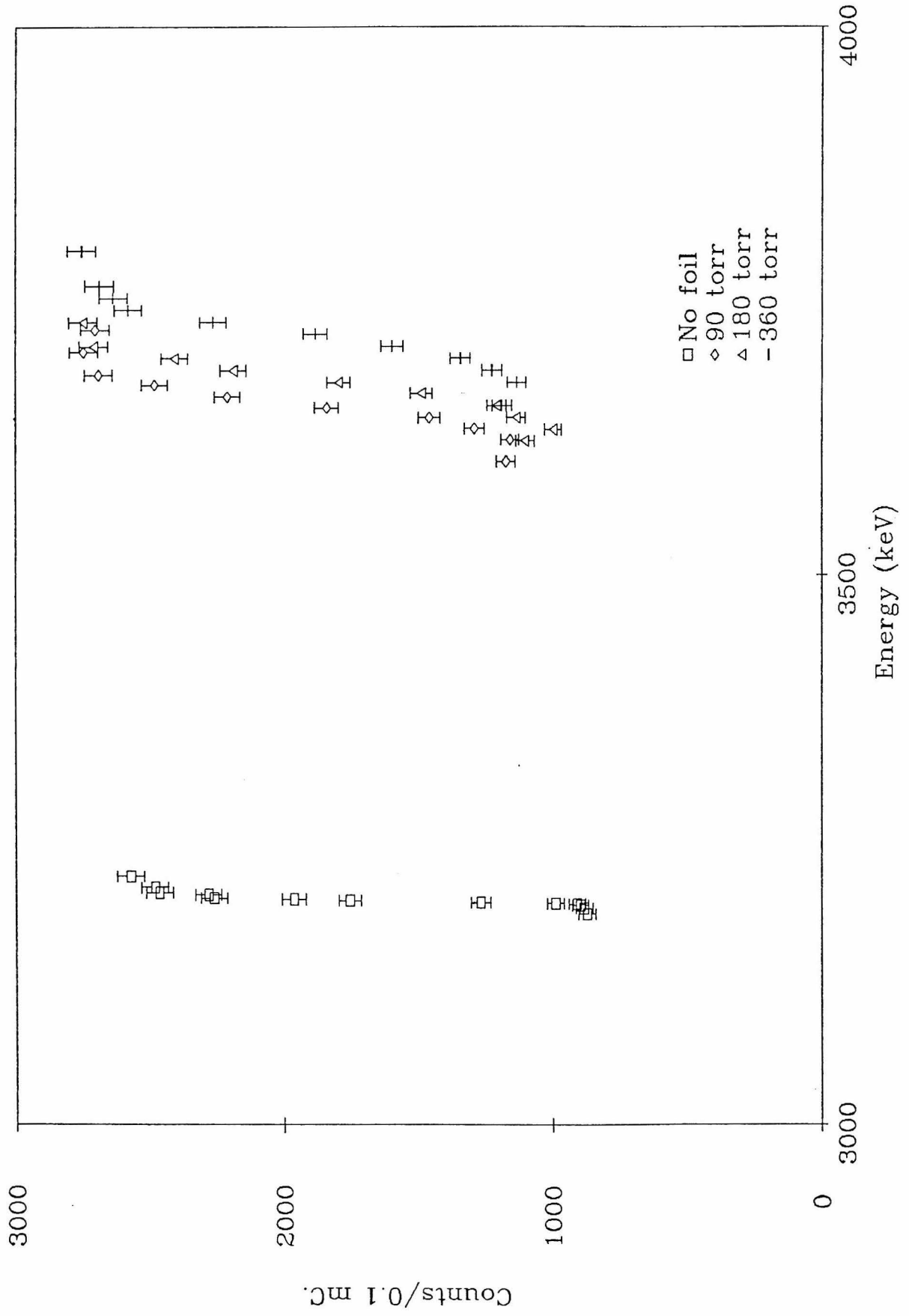


FIGURE 12

$^{14}\text{N}(\alpha, \gamma)^{18}\text{F}$ FOIL THICKNESS MEASUREMENTS

These curves show the excitation functions for the reaction $^{14}\text{N}(\alpha, \gamma)^{18}\text{F}$ with an α beam on a nitrogen target in the gas cell using the same entrance foil which was used in the $E_{cm}=947$ keV measurement. The two curves represent target pressures of 180 and 360 torr respectively. The vertical line represents the measured energy of the resonance (Ro73).

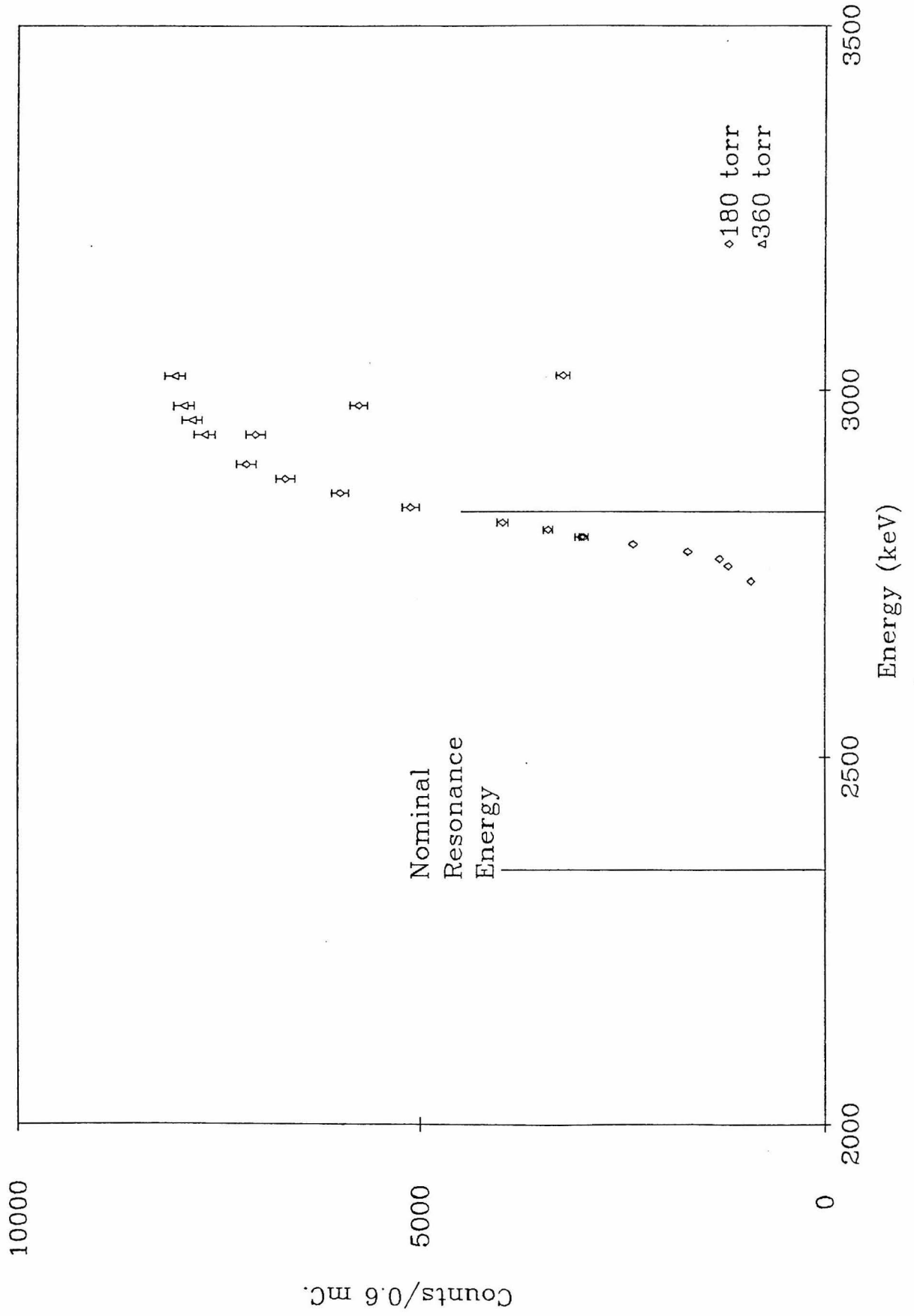


FIGURE 13
DIRECT-CAPTURE γ -RAY SPECTRA

Spectra of the direct-capture γ rays are shown for $E_{cm}=166$ keV (Run **P**), 347 keV (Run **D**) and 507 keV (Run **T**). The indicated γ -ray transitions are:

- a: γ_0 , direct capture to the ground state of ${}^7\text{Be}$
- b: γ_{429} , first excited state to ground state transition in ${}^7\text{Be}$
- c: γ_1 , direct capture to the first excited state of ${}^7\text{Be}$
- d: 511 keV, annihilation radiation
- e: 1460 keV, ${}^{40}\text{K}$ decay background
- f: 2614 keV, first excited state of ${}^{208}\text{Pb}$ from the ${}^{232}\text{Th}$ decay chain

Gamma Ray Spectra

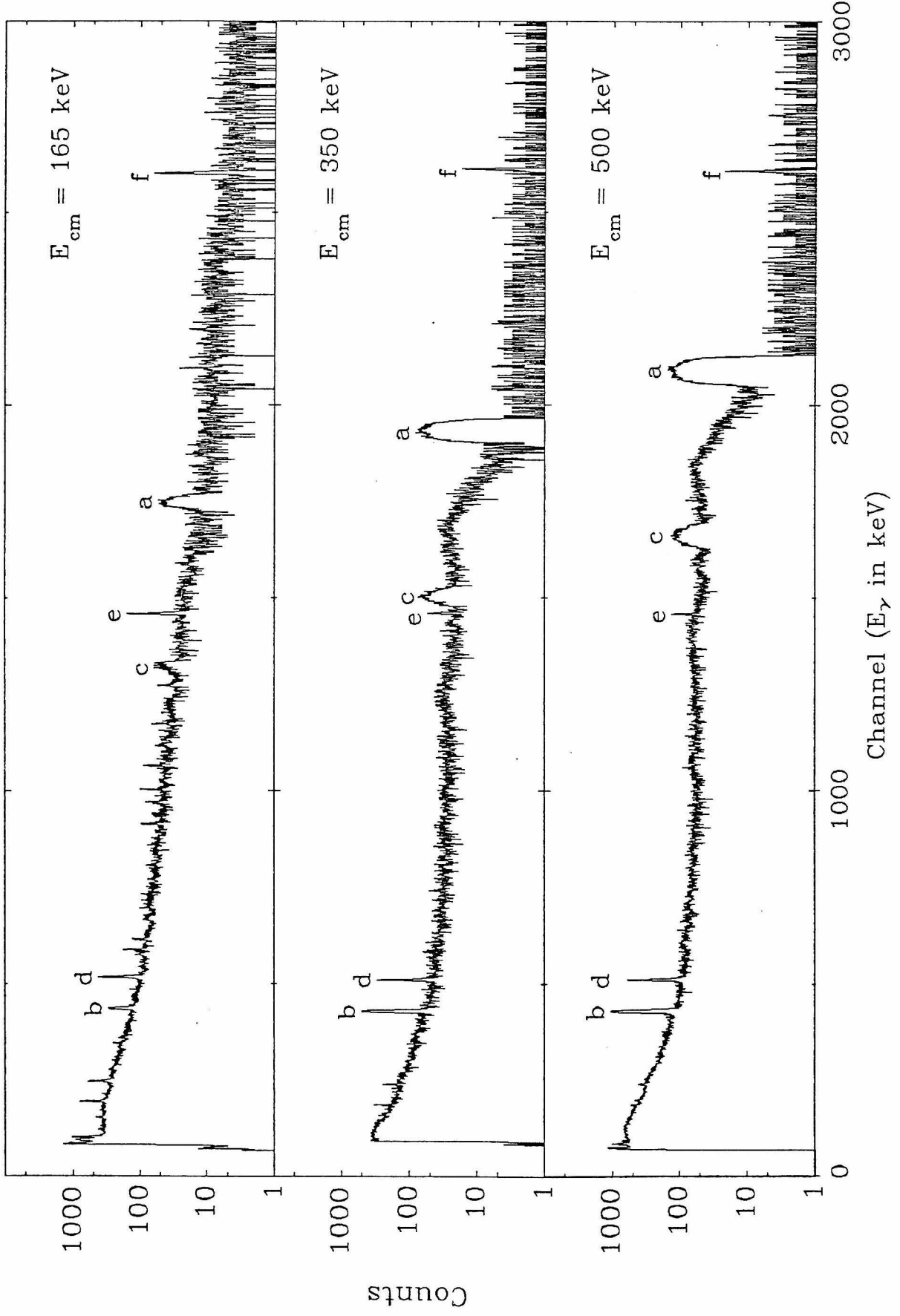


FIGURE 14
 γ -RAY DETECTION EFFICIENCIES

These four curves show the γ -ray detection efficiency in the windowless target as a function of position along the beam axis, relative to the center of Ge(Li) detector ($z=0$). The solid lines represent the best fit of the empirical function (given in table 2) to the experimental measurements.

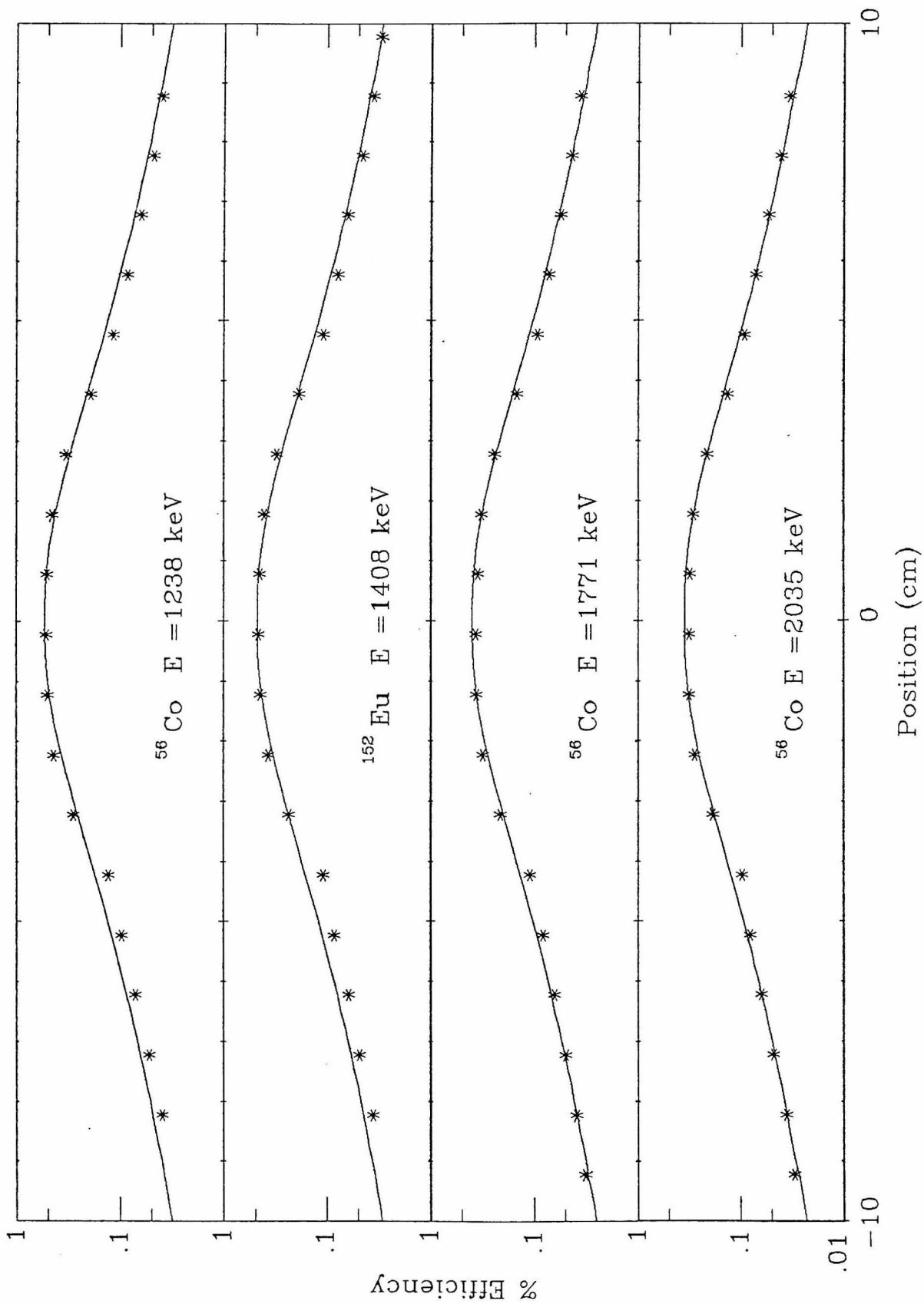


FIGURE 15
TOTAL DETECTION EFFICIENCY

The sum of the measured efficiencies at 1-cm intervals in the target is compared to the sum of the empirical efficiency function (see table 2) over the same positions. The resulting integrated efficiency is given in units of cm-%. The data points are from the ^{56}Co (squares) and ^{152}Eu (triangles) sources.

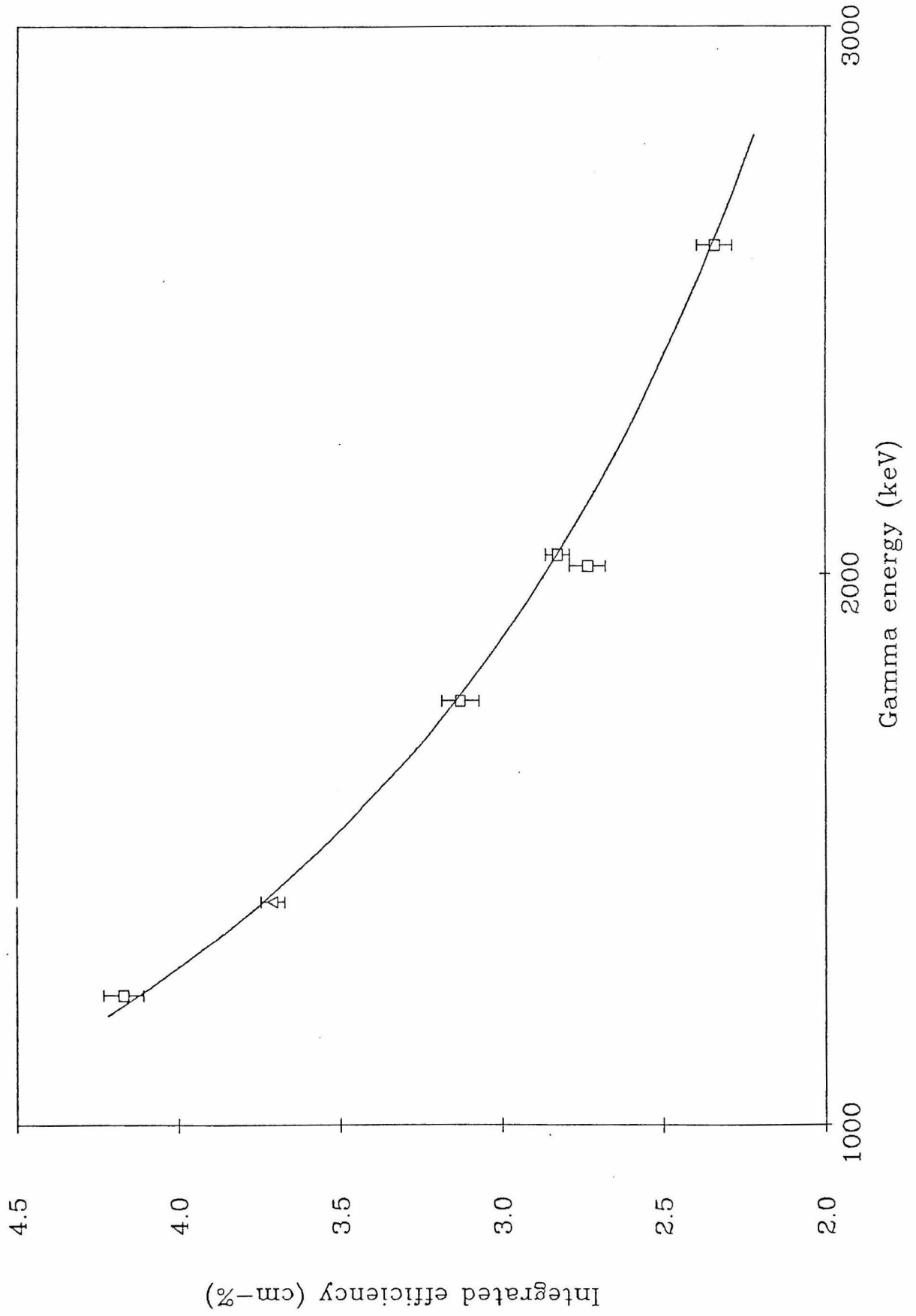


FIGURE 16
CATCHER FOIL SPECTRUM

The Ge(Li)-detector spectrum of the 144-hour count of the platinum catcher foil used in the $E_{cm}=1250$ keV activity measurement is shown. The inset shows the γ_{478} peak. The dotted line in the inset represents a 72-hour count of the entrance foil and the side foil. The total number of counts from the catcher foil is 2227 ± 86 . The number of counts in the side and entrance foil spectrum, using the same peak definition, is 27 ± 40 , consistent with zero.

Catcher Foil Spectrum

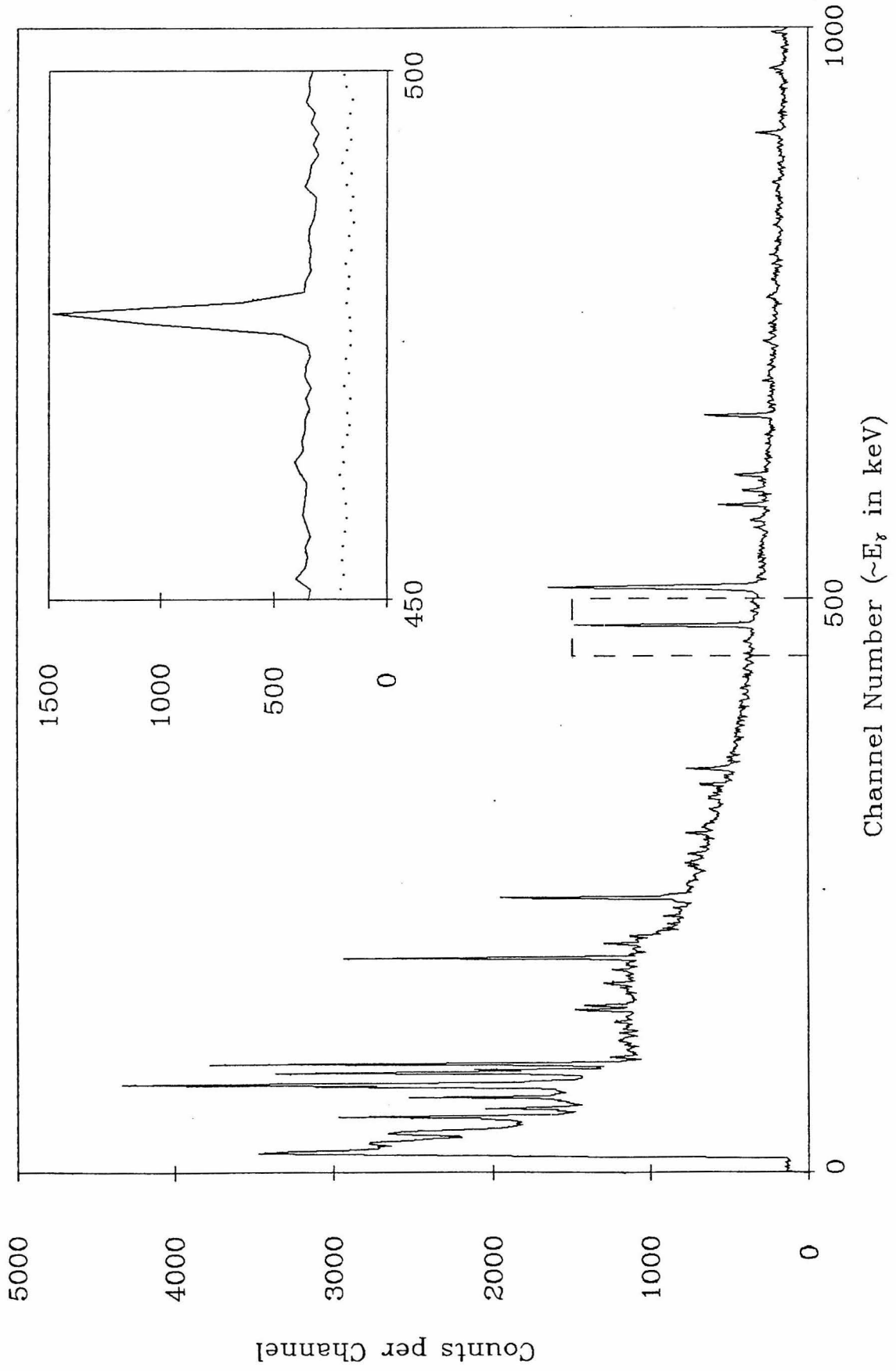


FIGURE 17
PROMPT γ -RAY SPECTRUM

The prompt γ -ray spectrum from the $E_{cm}=1250$ keV gas-cell measurement is shown along with the ^{24}Na source spectrum which was used for energy calibration.

Gamma Ray Spectra

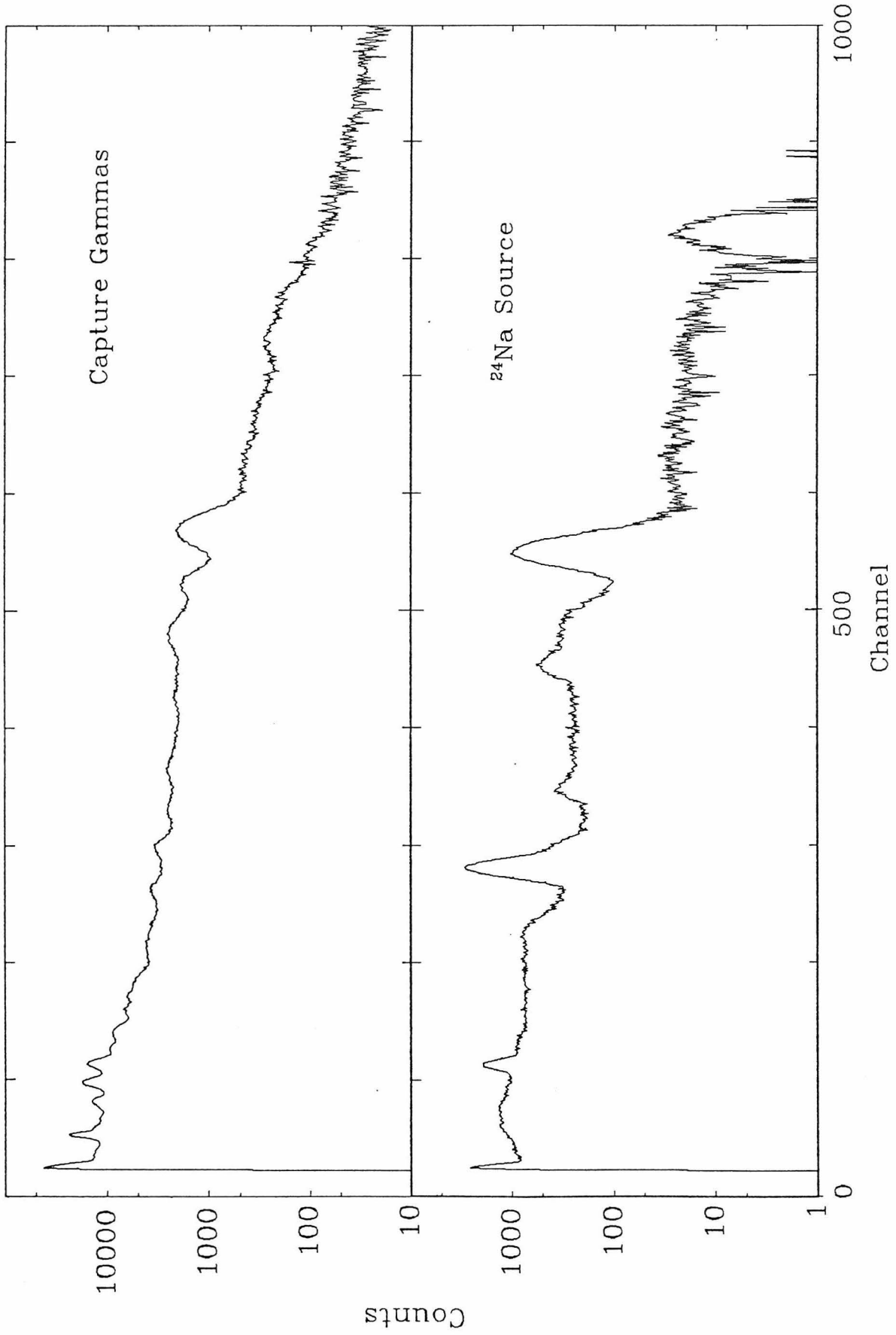


FIGURE 18
CROSS-SECTION FACTOR AND BRANCHING RATIO RESULTS

The results of these measurements are shown along with the best fit of the Tombrello and Parker (To63) calculation to the experimental data (solid curve) and the unnormalized resonating group calculation of Liu, Kanada and Tang (Li81, dashed curves). The normalized Tombrello and Parker branching-ratio curve is indistinguishable from that of Liu, Kanada and Tang.

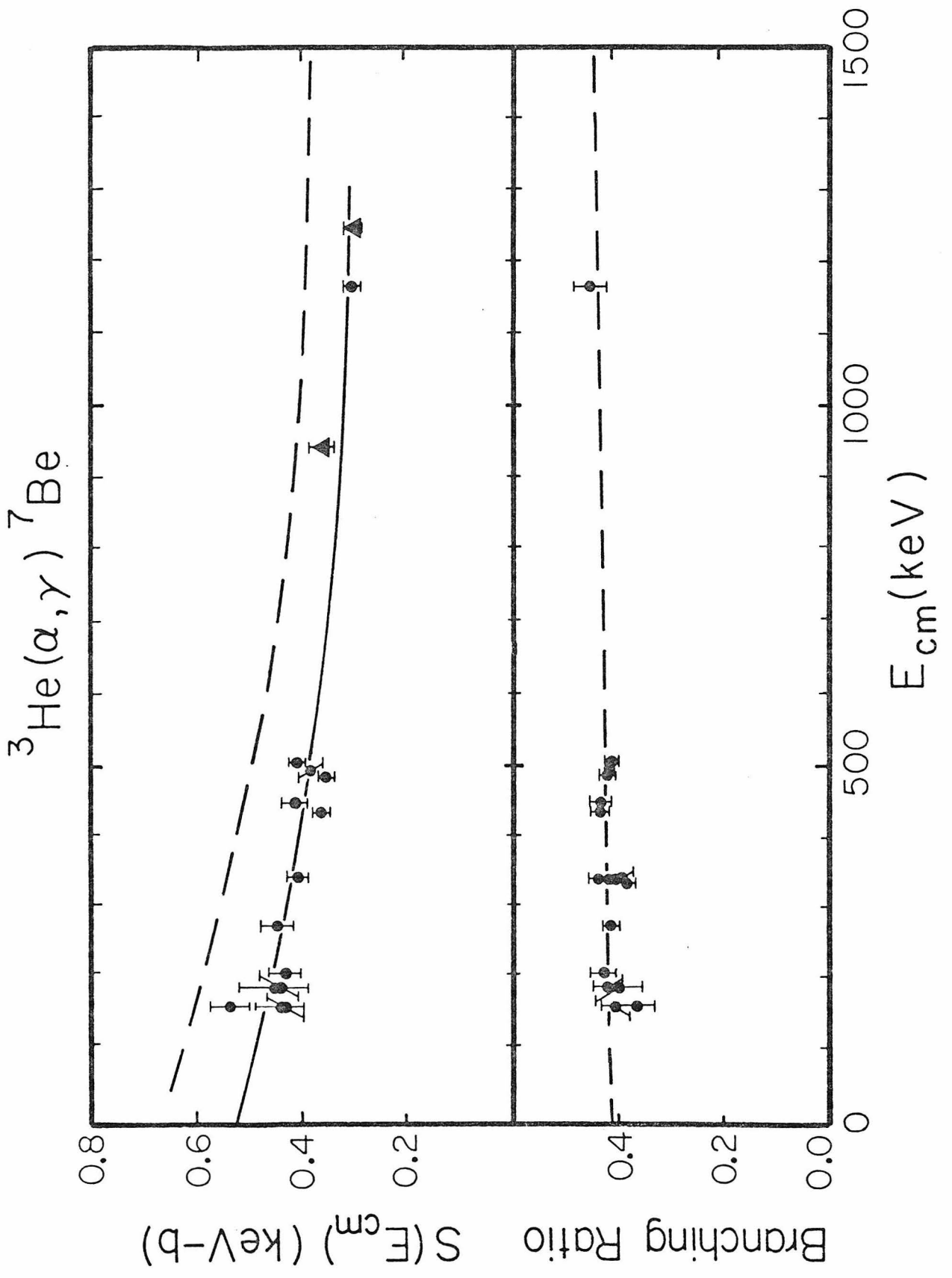


FIGURE 19
CALORIMETER

This is a full scale drawing of the calorimeter used to integrate the beam current in the windowless target. The body of the calorimeter was turned from a single block of copper.

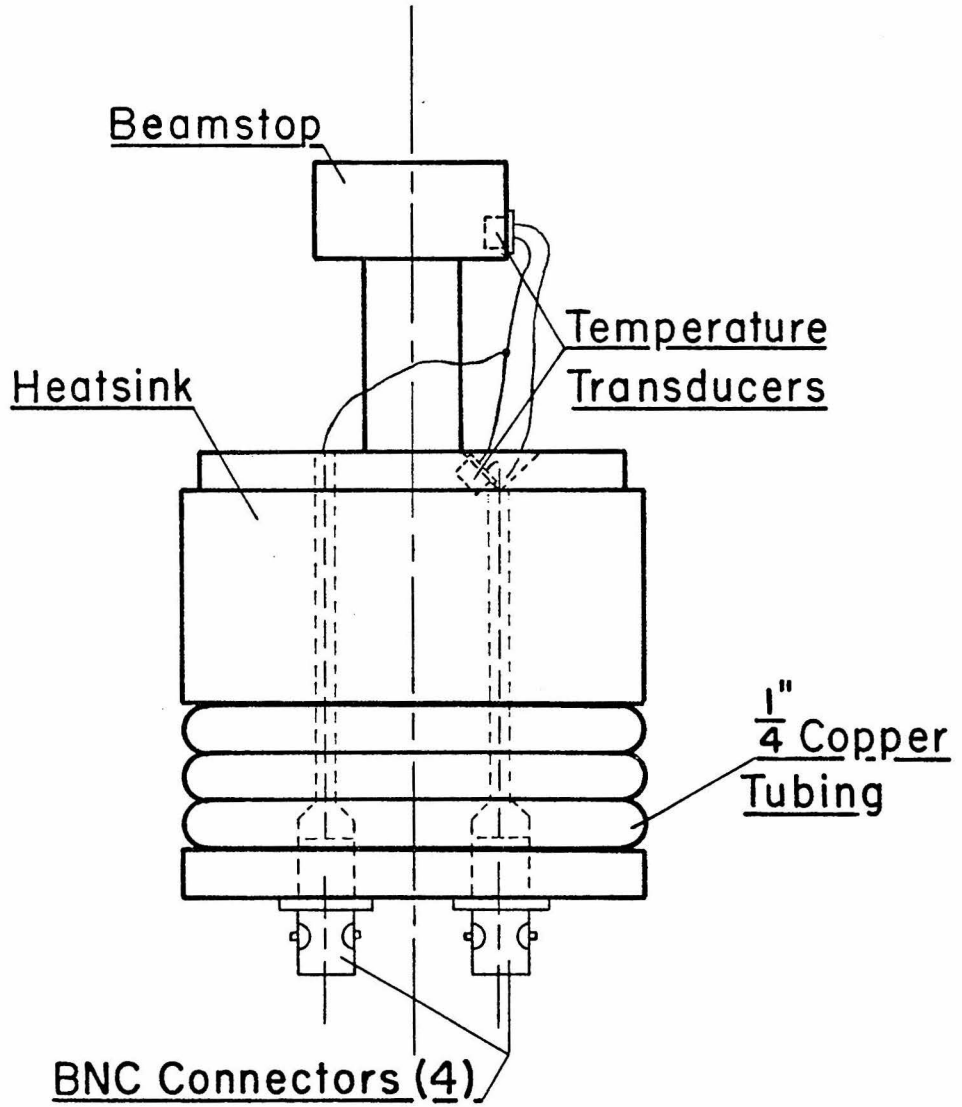


FIGURE 20
CALORIMETER CONTROLLER CIRCUIT

With the two temperature transducers placed in the bridge circuit as shown, the current flowing across the bridge will be proportional to the temperature difference, $T_2 - T_1$, between the beamstop and the heatsink. The $1\text{ k}\Omega$ variable resistor allows the circuit to be accurately zeroed. The $1\text{ k}\Omega$ resistors in series with the transducers allow the temperatures of the beamstop and the heatsink to be monitored; the voltage drop across these resistors in mV is equal to the kelvin temperature of the corresponding transducer.

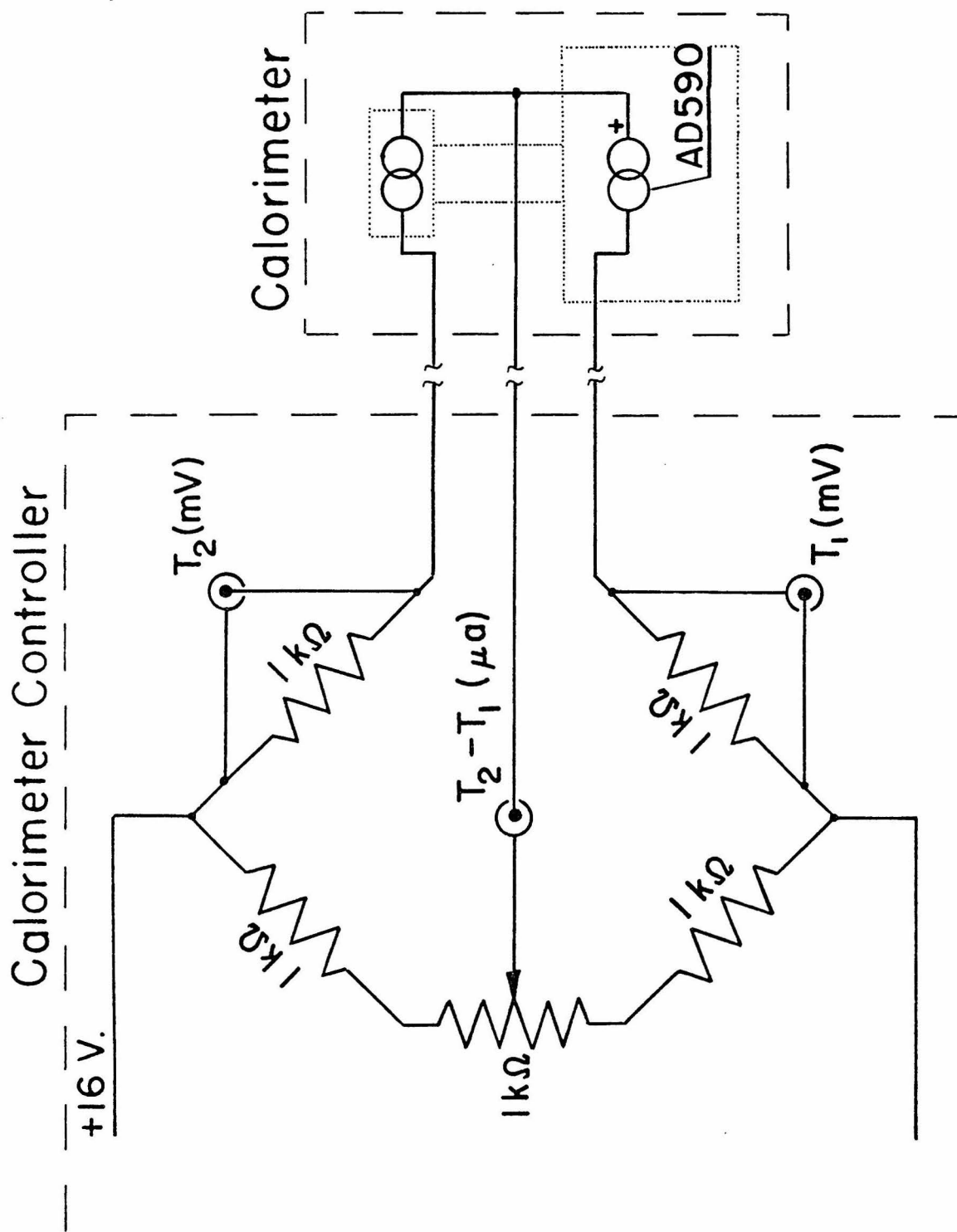


FIGURE 21
CALORIMETER CURRENT DECAY

A $32 \mu\text{A}$ beam of $401 \text{ keV } ^4\text{He}^+$ ions was turned on at $t=0$ sec and off at $t=106$ sec. The resulting beam current and calorimeter current are plotted in this graph as a function of time. The calorimeter current shows the expected logarithmic decrease, with a characteristic time constant of 26 sec.

Calorimeter Current Decay

